JPL Document D-60326

Exoplanet Interferometry Technology Milestone #3 Report

Broadband Starlight Suppression Demonstration

Editors:

R. D. Peters, R. O. Gappinger, P. R. Lawson, and O. P. Lay

February 2, 2009
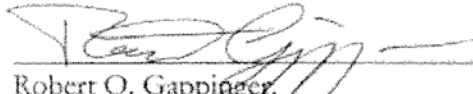
Approvals

Released by

(signature)   2/2/2009

Robert D. Peters,
Adaptive Nuller Testbed Cog. E.

(signature)   2/2/2009

Robert O. Gappinger,
Achromatic Nulling Testbed Cog. E.

Approved by

(signature)   2/2/2009
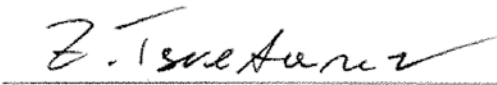
Peter R. Lawson,
Exoplanet Interferometry Technology Manager, JPL

(signature)   2/2/09

Michael Devirian
Exoplanet Exploration Program Manager, JPL.

(signature)   02/09/09

Zlatan Tsvetanov   _Technology_
Exoplanet Exploration Program Scientist, NASA HQ

(signature)   02/09/09

Lia LaPiana
Exoplanet Exploration Program Executive, NASA HQ

Table of Contents

Exoplanet Interferometry Technology

Milestone #3 Report
Broadband Starlight Suppression Demonstration

1. Objective

This document reports the achievement of Exoplanet Interferometry Technology Milestone #3, a demonstration of broadband starlight suppression in the mid-infrared. We review the milestone specification from the Milestone Whitepaper (October 10, 2007), summarize the experiments performed in the Adaptive Nuller testbed, detail the procedures and analysis of the resulting data, and describe and present the data itself. For completeness, an appendix is included that documents the performance of the Achromatic Nulling Testbed.

2. Introduction

The intent of this technology milestone was established in the TPF-I Technology Plan (JPL Pub. 05-5, June 2005) to gauge the developmental progress of the TPF-I project and its readiness to proceed from pre-Phase A to Phase A. Completion of this milestone is here documented by the Project, after having been reviewed by the External Independent Readiness Board (EIRB), and approved by NASA Headquarters. The milestone described here addresses broadband starlight suppression.

Milestone #3: Broadband Starlight Suppression

Using either the Adaptive Nuller or the Achromatic Nulling Testbed, demonstrate that mid-infrared light in the 7–12 µm range can be suppressed by a factor of $\geq 10^5$ over a waveband of $\geq 25\%$. This demonstrates the approach to broadband starlight suppression (dimming of light across a range of wavelengths) needed to characterize terrestrial planets for habitability. Flight-like nulls are to be demonstrated at room (non-flight) temperature. *Milestone TRL 5.*

The 10^5 suppression requirement is sufficient to reduce the residual starlight photon rate to below the background level set by the local zodiacal emission. It is worthwhile noting that the Sun-Earth flux ratio is ~10^7 at 10 µm, and further noise rejection is necessary to achieve a detection. This additional rejection is realized through a combination of phase chopping, the fact that the residual starlight is diluted over many pixels in the synthesized image, and the use of a spectral fitting technique that isolates the planet signal (Lay 2006). Although this additional rejection is not addressed by this Milestone, it will be demonstrated by the Planet Detection Testbed and is the subject of Milestone #4 (chopping and averaging) and Milestone #5 (spectral fitting).

A two-beam nuller is the basic building block of all flight architectures that have been considered so far. Four approaches to achromatic phase shifting have been investigated at JPL, with the aim of demonstrating, through one of the approaches, two-beam nulling to a level of 1 part in 100,000 with a 25% bandwidth. These methods are as follows: (1) using pairs of dispersive glass plates to introduce a wavelength-dependent delay; (2) using a through-focus field-flip of the light in one arm of the interferometer; (3) using successive and opposing field-reversals on reflection off flat mirrors in a

periscope arrangement; and (4) through adaptive nulling. The first two methods were tested in the Achromatic Nulling Testbed (ANT) prior to 2006. The third approach was then commissioned for the ANT (using periscope mirrors) and was evaluated beginning in 2005. The fourth approach, adaptive nulling, was the subject of TPF-I Milestone #1 that demonstrated mid-infrared amplitude and phase compensation over a broad band. The Adaptive Nuller performed so well that a single-pixel detector was included in the testbed specifically for broad-band nulling experiments.

Both the ANT and the Adaptive Nuller testbeds worked toward Milestone #3, which is the subject of this Report. The criteria of Milestone #3 were specifically drafted to allow either testbed to accomplish this Milestone; the Milestone would be deemed complete with the first qualifying results from either testbed, and it was not made mandatory that both testbeds arrive at the same performance level. Although the ANT was originally designed with Milestone #3 specifically in mind, its performance was eventually surpassed by the Adaptive Nuller in May of 2007. The Adaptive Nuller seemed sufficiently promising that in February 2008 work with the ANT was halted, and the testbed was decommissioned. The results achieved by the ANT will appear in the journal Applied Optics as an experimental evaluation of mid-infrared achromatic phase shifters (Gappinger et al. 2009). A copy of the paper is attached in Appendix A. This Milestone Report presents the milestone data recorded with the Adaptive Nuller.

The Adaptive Nuller was described in detail in the publication by Peters, Lay & Jeganathan (2008). It is only briefly reviewed here.

Note that all of the designs under consideration for TPF-I include a single-mode spatial filter through which the combined light is passed before being detected. The wavefront from the star is incident on the collecting apertures of the instrument and delivered by the respective beam trains to a central beam combiner that couples the combined light into a single-mode filter. With just a single mode for each polarization state, the problem of nulling the on-axis light is simplified. Higher order wavefront aberrations that would reduce the visibility of the fringes (depth of the null) are rejected by the spatial filter. Small errors in tilt in each arm of the interferometer thus translate into small errors in received intensity. Nulling testbeds that use single-mode spatial filters need not adjust wavefront errors across each pupil, as these are rejected independently by the filter itself. For further information about the mid-infrared spatial filters to be used with TPF-I, the interested reader is referred to Ksendzov *et al.* (2007) and Ksendzov *et al.* (2008).

2.1.   Adaptive Nuller

The adaptive nuller uses a broadband thermal source to generate light with a spectral width $> 3\ \mu m$ centered at a wavelength of $\sim 10\ \mu m$. This light is put through a simple interferometer with one arm holding the adaptive nuller components, and the other serving as a reference arm. There will be intensity and phase dispersion in this interferometer due to normal manufacturing tolerances which are compensated by the adaptive nuller.

There is no achromatic phase shifter between the arms of the interferometer. The Adaptive Nuller introduces a half-wavelength delay (approximately 5 microns path difference) and adjusts the residual path difference at each wavelength using the adaptive compensator. The adaptive nuller measures the intensity and phase dispersion as a function of intensity and phase differences between the arms of the interferometer versus wavelength. From this measurement, the required adjustments to

the deformable mirror (DM) actuator are calculated and the correction is applied. Through an iterative process the intensity dispersion is corrected to $\leq$ 0.2% rms (1 σ) intensity difference between the arms. The phase dispersion is corrected so that it is $\leq$ 5nm rms (1 σ).

The layout of the Adaptive Nuller is shown in Fig. 1. This layout was slightly modified for this milestone. A single-pixel detector was included at the output of the interferometer so that all the light, normally dispersed in a spectrometer, could be re-directed by a flip-mirror to be focused onto a single pixel for the measurement of a time-series of the null.
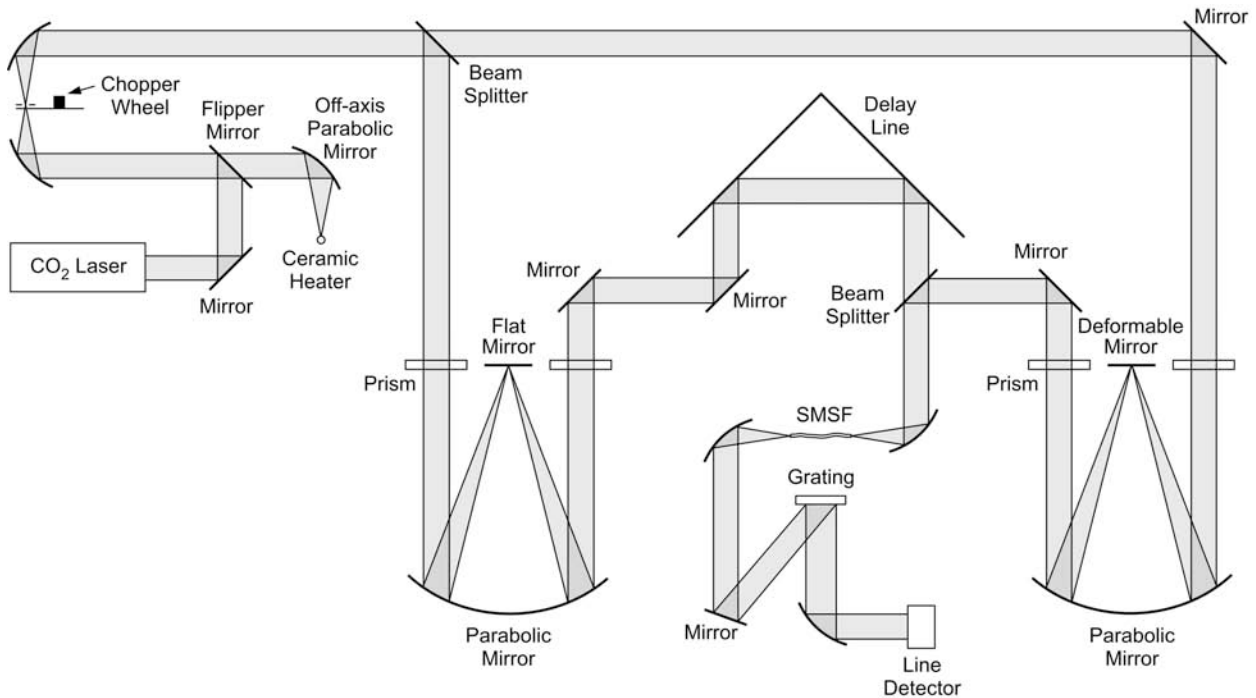

Figure 1: Layout of the Adaptive Nuller, showing the laser and thermal source, chopper wheel, beam splitter and beam combiner, as well as the delay line, the adaptive compensating arm (right, having a parabolic mirror with a deformable mirror at its focus), and the reference arm (left, having a parabolic mirror with only a flat mirror at its focus). The Single Mode Spatial Filter (SMSF) is shown prior to a grating and line detector. For this milestone, the above layout was slightly modified after the SMSF to include a flip-mirror that could redirect light to a single-pixel detector. The single-pixel detector was used to measure the broadband null depths that are the subject of this report.

In addition, an acoustic enclosure was installed over the testbed to reduce the ambient acoustic noise. Such enclosures are used for industrial applications to either reduce the noise of loud equipment or provide a noise-isolated environment in which to work. Figures 2 and 3 show the Adaptive Nuller testbed before and after the installation of the enclosure. The enclosure provided more than 15 dB of acoustic noise suppression and improved the achievable rejection ratios (inverse of the null depth) from about 80,000:1 to slightly above 100,000:1. Although the null depths only exceeded the milestone requirement by a slim margin, they were extremely stable and repeatable. Of the nulling experiments that were conducted for this milestone, not a single experiment failed to meet the criteria because of the achievable null depth: an early attempt failed because a dewar warmed up 5.5 hours into the experiment, and one subsequent run failed because a circuit breaker tripped that provided high-voltage to the DM.
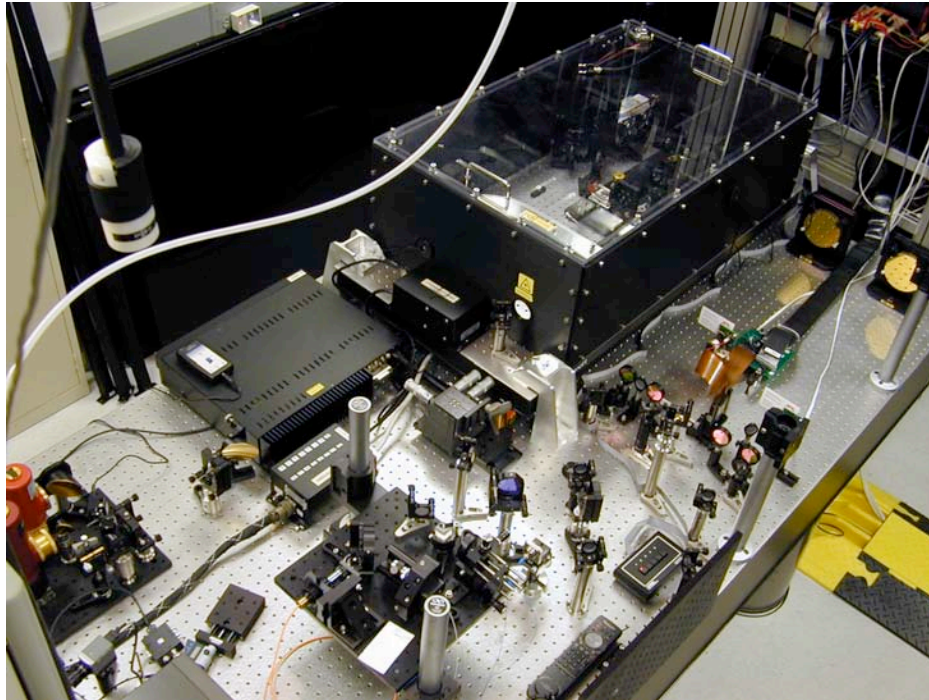
Figure 2: View of the Adaptive Nuller prior to the installation of its acoustic enclosure (April 14, 2008).

Figure 3: View of the Adaptive Nuller after the installation of its acoustic enclosure (January 29, 2009). The enclosure was installed for this milestone and reduced the measured ambient acoustic noise by more than 15 dB. The testbed PI, Robert Peters, is shown in the foreground. The enclosure was manufactured by DB Engineering.

2.2. Differences between Flight and Lab Demonstration

Based on discussions from past Milestone reviews, we note here several important differences between the lab demonstrations and the baselined flight implementation: 2 beams vs. 4 beams, spacecraft dynamics, air vs. cryo-vacuum, and the source intensity. Each is addressed briefly below.

Table 1. Comparison of Flight Requirements with Pre-Phase A Testbed Specifications and Actuals

Parameter	Flight Performance	Achromatic Nulling Tesbed[1,2]	Planet Detection Testbed	Adaptive Nuller[3]
Null depth	1×10^{-5}	1×10^{-5}	1×10^{-5}	1×10^{-5}
Amplitude control	0.13%	Derived	0.12%	0.2% (static)
Phase control	1.5 nm	Derived	2 nm	5 nm (static)
Stability timescale	50,000 s +	21,600 s	5,000 s	21,600 s
Bandwidth	7–17 µm	25 % (8.3–10.7 µm)	λ = 10.6 µm	30 % (8.2–11.6 µm)

[1] The Milestone #3 criteria are listed here: mean null $\leq 1 \times 10^{-5}$, bandwidth $\geq 25\%$ (with actual bandwidth of the testbed noted in parentheses), measurements to span $\geq$ 6-hour.

[2] The final results from the Achromatic Nulling Testbed are given in the paper by Gappinger et al. (2009).

[3] The Milestone #1 criteria are listed here (with actual bandwidth noted in parentheses). Further details can be found in the paper by Peters et al. (2008). Note the specifications of the Adaptive Nuller are compatible with the Milestone #3 criteria.

2 beams vs 4 beams: The baseline array configuration for TPF-I combines 4 beams to form the null. This is implemented in two stages: pair-wise nulling followed by cross-combination of the two nulled beams. Since all the nulling occurs at the first stage, the two-beam broadband lab demonstrations of the Achromatic Nulling Testbed and the Adaptive Nuller provide a meaningful representation of achievable flight performance. Four-beam combination will be demonstrated in the lab with the Planet Detection Testbed.

Spacecraft dynamics: A control system is required in flight to stabilize the beams against motions of the spacecraft. It is assumed that the tip/tilt, optical path difference, and shear of each beam is stabilized at the input to the nuller. The lab demonstration has active path length control only. The active stabilization of 4 beams is demonstrated in the Planet Detection Testbed.

Polarization: In the case of the Adaptive Nuller, the flight system will split the two linear polarization states and correct each independently. The Adaptive Nuller *lab* demonstration operates on unpolarized light without splitting the components, and therefore has fewer degrees of freedom to make a correction.

Cryo-vacuum: The flight system operates in vacuum at low temperature (~ 40 K), compared to the ambient air environment of the lab demonstration. The lab is a more challenging disturbance environment, and the room temperature thermal background is a significant source of noise in the experiment. Future engineering will have to address the need for a cryogenic Deformable Mirror (DM) in a version of the Adaptive Nuller that will operate in vacuum at low temperature, as well as the need for cryovacuum compatible pathlength control and dispersion compensation. Other aspects of the design, including the cryogenic stability of the periscope monolith, may also be investigated.

Source intensity: The broadband sources in the lab provide a higher photon flux than the target stars to be observed by the mission. This is offset by the higher detector readout noise in the lab. The goal of this milestone is to demonstrate the fundamental broadband null depth that can be achieved, which is independent of the source intensity. If a 10^{-5} null is measured with the bright lab source, then the same null would be obtained if the source brightness were suddenly reduced to the level expected from a typical star—but it then wouldn't be measurable in the presence of lab detector noise and the room-temperature background.

3. Milestone Procedure: Adaptive Nuller

3.1. Definitions

Milestone #3, the broadband starlight suppression demonstration, requires measurement of the null depth or rejection ratio in an interferometer. In the following paragraphs we define the terms involved in this process, spell out the measurement steps, and specify the data products.

3.1.1. "Star".   We define the "star" to be a 75 μm diameter pinhole illuminated with ceramic heater thermal source with a temperature of 1250–1570 K. This "star" is the only source of light in the optical path of the adaptive nuller. It is a stand-in for the star signal that would have been collected by the telescope systems in TPF-I; however it is not intended to simulate any particular collector design or expected flux.

3.1.2. "Dispersion". We define dispersion to be the difference in either amplitude *or* phase as a function of wavelength between the two arms of an interferometer.

3.1.3. "Algorithm". We define the "algorithm" to be the computer code that takes as input the measured amplitude and calculated phase dispersion, and produces as output a voltage value to be applied to each element of the DM, with the goal of reducing the dispersion.

3.1.4. "Cross coupling". We define cross coupling to be the unintended adjustment of phase while amplitude is being corrected or the unintended adjustment of amplitude while phase is being corrected.

3.1.5. "Monochromatic source". We define a monochromatic source to be a carbon dioxide laser with an operating wavelength near 10 μm with narrow spectral line width that is co-aligned with the "star" source. As we are only able to control dispersion, we do not expect to achieve a null deeper than the null obtained with this source.

3.1.6. "Active metrology". We define active metrology as a system which uses a laser at 1.3 μm wavelength to measure the difference in optical paths of the two arms of the interferometer. This information is then fed back to the delay line control to maintain a set path difference.

3.1.7. "Spectrometer". We define a spectrometer to be a device to measure intensity as a function of wavelength. The device consists of a grating to disperse the incoming light. The dispersed light is then focused by an off-axis parabola onto a linear mercury cadmium tellu-

ride array with 16 elements. Each element produces a voltage proportional to the intensity in a wavelength range selected by the grating. The output voltages are then sent through a multiplexer to a lock-in amplifier with an integration time set from 100 ms to 30 s depending on the signal level. The output of the lock-in amplifier is then read by the computer for each element of the linear array. Noise may be reduced by averaging up to 10 frames taken from the spectrometer.

3.1.8. **"Single Pixel Detector".** We define the single-pixel detector to be a single mercury cadmium telluride detector, which can be used in parallel with the spectrometer. A pick-off mirror placed before the grating directs the undispersed light from the single mode spatial filter to be focused on this detector.

3.1.9. "**Adaptive nulling**". We define the process of adaptive nulling to be the following 4 step process, iteratively repeated for as many cycles as necessary to reach the desired level of amplitude and phase dispersion.
a) Measure the intensity dispersion in the interferometer by measuring the intensity spectrum of each arm independently while shuttering off the other arm.
b) Compute the required tilts to equalize the intensity difference in each channel of the deformable mirror (DM) and apply these voltages.
c) Calculate the phase dispersion in the interferometer by actuating the delay line several fringes off the null and measuring the dispersed spectral fringes with the spectrometer and applying an algorithm to the output.
d) Compute the required piston settings to equalize the path lengths in each channel of the DM and apply these voltages.

3.1.10. **"Null Depth".** We define the null depth to be the ratio of the peak signal caused by constructive interference in the interferometer to the null signal caused by destructive interference in the interferometer.

3.1.11. **"Rejection Ratio".** We define the rejection ratio to be the inverse of the null depth.

3.2. Measurement of the null

Each null measurement is obtained as follows after intensity and phase correction have been applied:

3.2.1. The delay line is actuated by the computer to locate the approximate position of the minimum integrated power as measured on the single pixel detector.

3.2.2. The delay line is then actuated by the computer to the peak integrated power. The set point is slowly scanned on the active metrology to locate the peak. The peak integrated power is used to normalize the null depth.

3.2.3. The delay line is then actuated by the computer back to the null.

3.2.4. The metrology set point is then slowly scanned by the computer to find the minimum integrated power as measured on the single-pixel detector.

3.2.5. The active metrology system can then be used to hold this position to measure the time evolution of the null.

3.3. Milestone #3 Validation Procedure

3.3.1. All DM actuators are set to half their control range.

3.3.2. The active metrology system and the star are turned on. The delay line is then actuated by the computer to locate the null position.

3.3.3. An initial uncorrected null is measured as described in Sec. 3.2.

3.3.4. The delay line is actuated away from the null by several fringes and adaptive nulling is performed to correct the measured intensity dispersion to $\leq$ 0.2% and correct the measured phase dispersion to $\leq$ 5nm.

3.3.5. The delay line is actuated by the computer to locate the null position.

3.3.6. The corrected null is measured as described in Sec. 3.2

3.3.7. To measure the stability, step 3.3.6 is repeated while the DM voltages are held constant and the active metrology holds the delay line position to measure the time evolution of the null.

3.3.8. The following data are to be archived for future reference: (a) raw spectrometer output of null and peak of star before and after correction, (b) phase and intensity dispersion before and after correction, and (c) raw output of the null and peak measured at each time interval after correction.

3.3.9. The following data are to be presented in the final report: (a) Plot showing peak and null as a function of wavelength before and after correction, (b) plot of time series of null depth.

3.3.10. Repeat steps 3.3.1–3.3.7 on two more occasions on different days, with at least 48 hours between each demonstration.

4. Success Criteria

The following is a statement of the 3 elements that must be demonstrated to close Milestone #3. Each element includes a brief rationale. The success criteria are common to both the Achromatic Nulling Testbed and the Adaptive Nuller. However, the Milestone criteria need only be met by one of the two testbeds in order to close the Milestone.

4.1 A null depth measured over a fractional bandwidth of $\Delta\lambda/\lambda \geq 25\%$, where the central wavelength, λ, lies in the range $7~\mu m < \lambda < 12~\mu m$.

Rationale: *The bandwidth is large enough to give confidence that a small number of instruments would be necessary to cover the full TPF-I science band of 7–18 μm.*

4.2   A time series showing mean null depth to be less than or equal to 1×10^{-5} observed in single or dual-polarization light for a 6 hour period. The mean null depth is defined as the average measured power at the null fringe over a contiguous 6 hour time period. The data from which the average is estimated will be a continuous data set, without gaps, that spans at least a 6-hour period. Although the null depth may be allowed to exceed 1×10^{-5} for long periods, the average as measured over the entire 6 hours must be less than or equal to 1×10^{-5}. The brightness of the experimental source need not be representative of a typical stellar source. The room temperature will be monitored but not controlled beyond the facility controls for the room.

Rationale: *The null depth to be demonstrated is the flight requirement and would allow planet signal extraction when methods of instability noise compensation are employed. As this milestone emphasizes broadband performance, a single-polarization measurement is sufficient; dual-polarization performance, if not demonstrated here, will be addressed in a subsequent milestone. The null depth is independent of the source brightness, and thus there is no requirement imposed for the use of representative light levels for this milestone. A representative science observation would require an array rotation period of 50,000 s (~14 hrs), and thus the time-series duration of 6 hrs demonstrates long-term stability of the system, approaching flight-level requirements.*

4.3   Elements 4.1 – 4.2 must be satisfied simultaneously on three separate occasions with at least 48 hours between each demonstration.

Rationale: *This provides evidence of the repeatability of the broadband starlight suppression.*

5. Certification Process

The Project will assemble a milestone certification data package for review by the EIRB. In the event of determination that the success criteria have been met, the project will submit the finding of the review board, together with the certification data package, to NASA HQ for official certification of milestone compliance. In the event of disagreement between the project and the EIRB, NASA HQ will determine whether to accept the data package and certify compliance or request additional work.

5.1. Certification Data Package

The milestone certification data package will contain the following explanations, charts, and data products.

5.1.1.   A narrative report, including a discussion of how each element of the milestone was met, an explanation of each plot or group of plots, appropriate tables and summary charts, and a narrative summary of the overall milestone achievement.

5.1.2.   Although the body of the report will document the performance of the testbed that met the milestone requirements, the report will also include an appendix to document the performance of the other testbed. This appendix is not included as part of the success criteria, but is for completeness and information only.

6. Lab Results

Here we describe how each element of the milestone was met, with an explanation of the data obtained, analysis of the data, and a narrative summary of the overall milestone achievement.

6.1. Fractional Bandwidth and Central Wavelength

Requirement 4.1 (see Section 4.1) states the minimum fractional bandwidth, $\Delta\lambda/\lambda$, and central wavelength, λ, that will be used for the experiments. The spectra shown in Figure 4 have been measured with and without a calibrated filter. This demonstrates the response across the 16 pixels on the line detector used for the adaptive compensation of amplitude and phase. The filter is used here as a reference only. When the experiments were conducted, there were no filters in place.
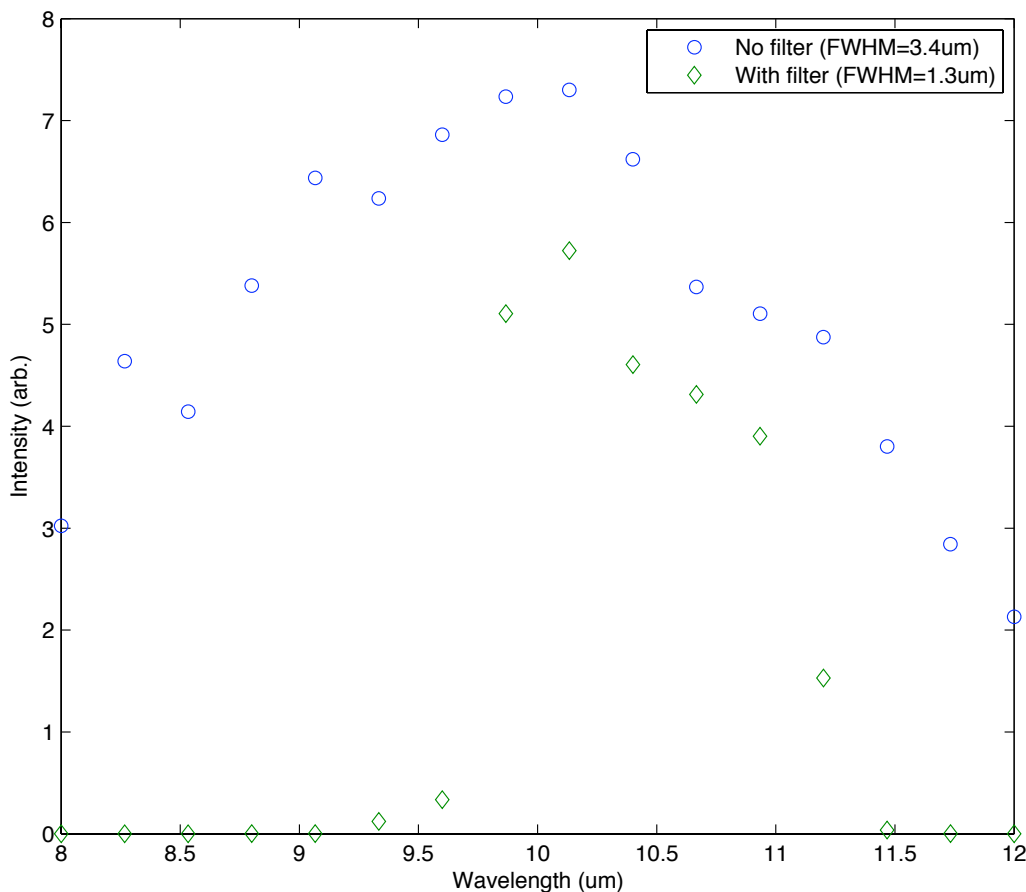

Figure 4: Measured intensity as a function of wavelength without a filter (blue open circles) and with a 1. 3 micron FWHM bandwidth filter (green open diamonds). The details of the reference filter are given in Figure 5. The above plot shows the response of the 16 pixels on the line detector used for adaptive compensation. The FWHM of the "No filter" bandwidth used for the experiments spans a wavelength range of 8.2 microns to 11.6 microns, with a central wavelength of 9.9 microns. This corresponds to a fractional bandwidth of 34% centered at $\lambda = 9.9$ micron, demonstrating that the fractional bandwidth and central wavelength criteria have been met by the experiment.
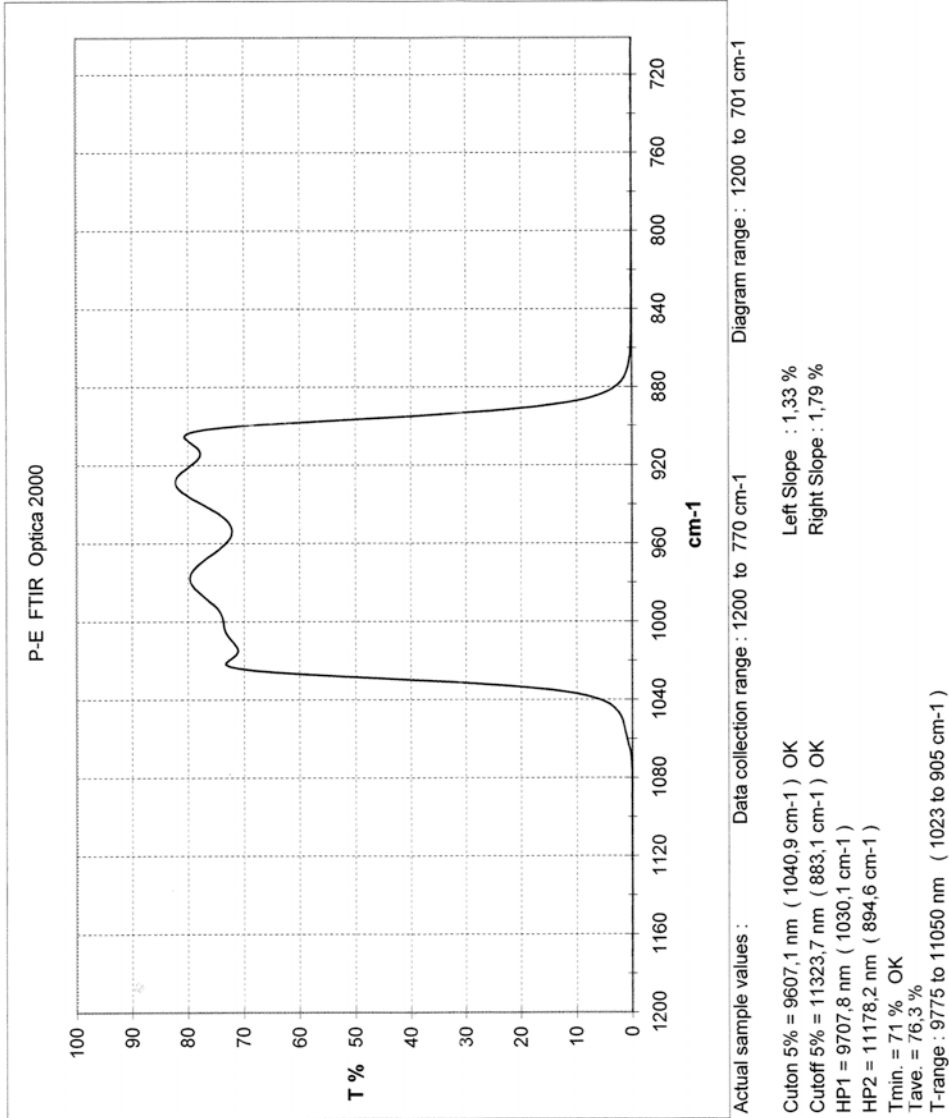
Figure 5: Data sheet for the reference filter cited in Figure 4.

When the nulling experiments were conducted, the light was re-directed to a single-pixel detector used to measure null depth. As shown in Fig. 4, the "No filter" spectrum peaks with an intensity of ~7.3. The Full-Width at Half Maximum (FWHM), measured at an intensity level of ~3.7, spans a wavelength range from 8.2–11.6 μm (3.4 μm bandwidth) with a central wavelength of 9.9 μm. The "No filter" response was the bandwidth actually used for the experiments. The FWHM of 3.4 μm and central wavelength of 9.9 μm correspond to a fractional bandwidth of 34%. The fractional bandwidth of 34% is greater than 25%, and central wavelength of $\lambda = 9.9$ μm is within the range of 7 μm $< \lambda <$ 12 μm. The fractional bandwidth and central wavelength thus meet Requirement 4.1 (Section 4.1). It should be noted as well that no polarizing filters were used in these experiments.

6.2.   Length and Timeline of Data Sets

Requirement 4.2 (see Section 4.2) states the required duration of the tests. Requirement 4.3 (see Section 4.3) states the required time line over which the nulling experiments are to be conducted. Table 2 indicates the times when data was taken and the total duration of each experiment. The data sets each have a duration longer than 6 hours. More than 48 hours elapses between data sets. The duration of the tests and their time-line thus meets the requirements as stipulated in 4.2 and 4.3.

Table 2. Acquisition dates and times for the three sets of measurements.

Data Set	Date	Start	End	Duration
1	12/10/2008	6:07 pm	12:18 am (12/11/2008)	6:11
2	01/09/2009	6:12 pm	12:20 am (01/10/2009)	6:08
3	01/15/2009	6:18 pm	12:22 am (01/16/2009)	6:04

6.3.   Mean Null Depth

Requirement 4.2 (see Section 4.2) also states the success criteria for null depth to be demonstrated. Requirement 4.2 states that the mean null depth, measured as the average over an entire 6-hour data set, must be less than or equal to 1×10^{-5}. We show here that this requirement has been met.

Figure 6 to Figure 11 show plots of the null depth measured as a function of time for data sets 1, 2, and 3. Data set 1 is shown in Figures 6 & 7. Data set 2 is shown in Figures 8 & 9. Data set 3 is shown in Figures 10 & 11. In each case the data is shown twice to illustrate the full scale of the null, but to also show fine variations in null depth at the level of 1×10^{-5}. It should be noted that the performance of the Adaptive Nuller only slightly exceeds the performance called out for in the Milestone criteria. Thus, in each plot the null depth is on average less than 1×10^{-5}, but for long periods also rises above that level. The criteria states that the *average* as measured across the entire 6-hour data set must be less than 1×10^{-5}; this level of performance has indeed been demonstrated in each case.
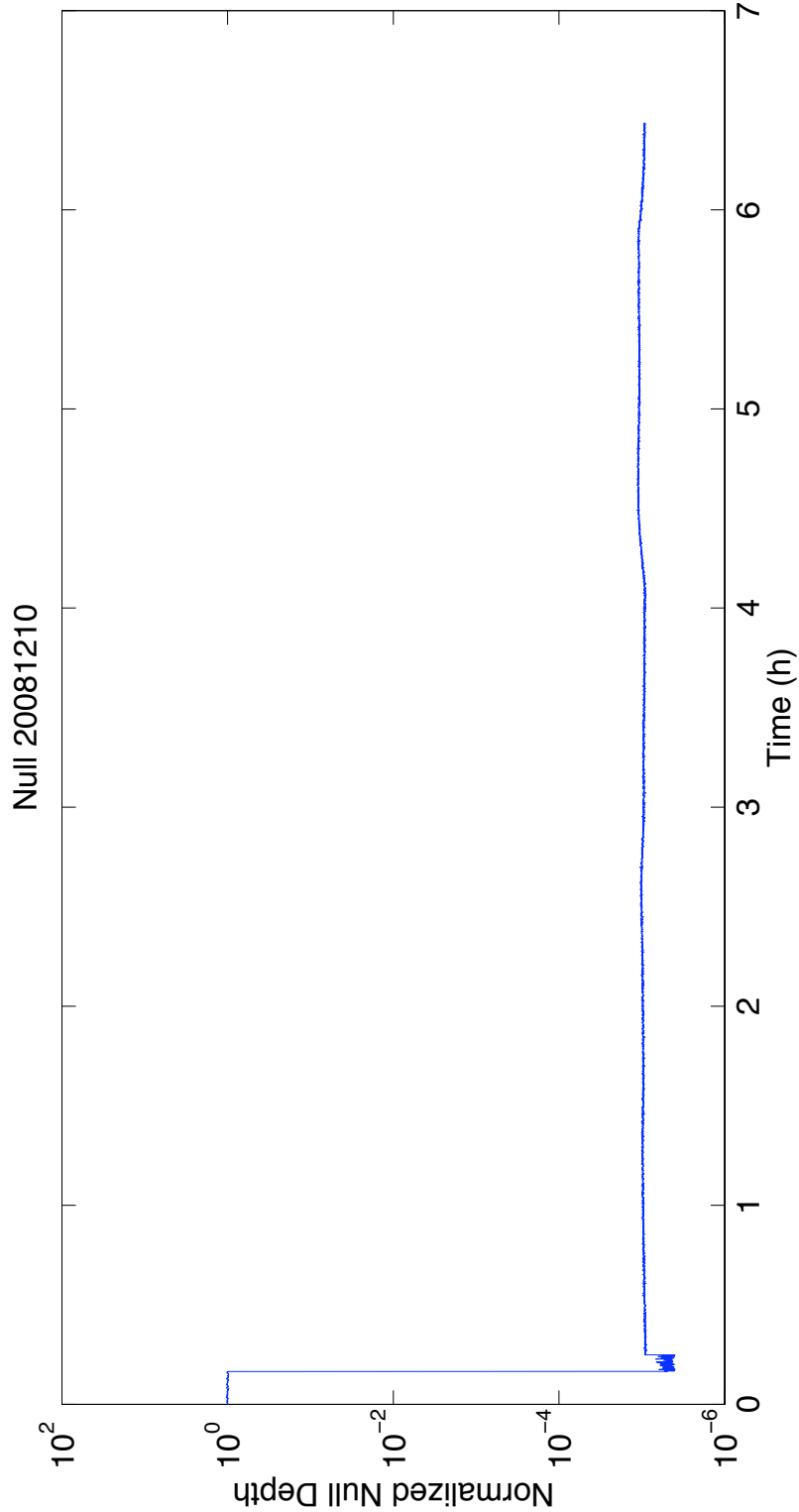
Figure 6: Measured null depth as a function of time, as measured on 10 December 2008. This plot shows the data from the time the experiment was initialized, through until the end of the data taking. The data begin with a measurement of the reference level (at 1×10^0), then a measurement of the noise floor with both shutters off (the dip below 1×10^{-5}), then both shutters open and the nulling data are recorded. An expanded view of the subsequent data is shown in Fig. 7.
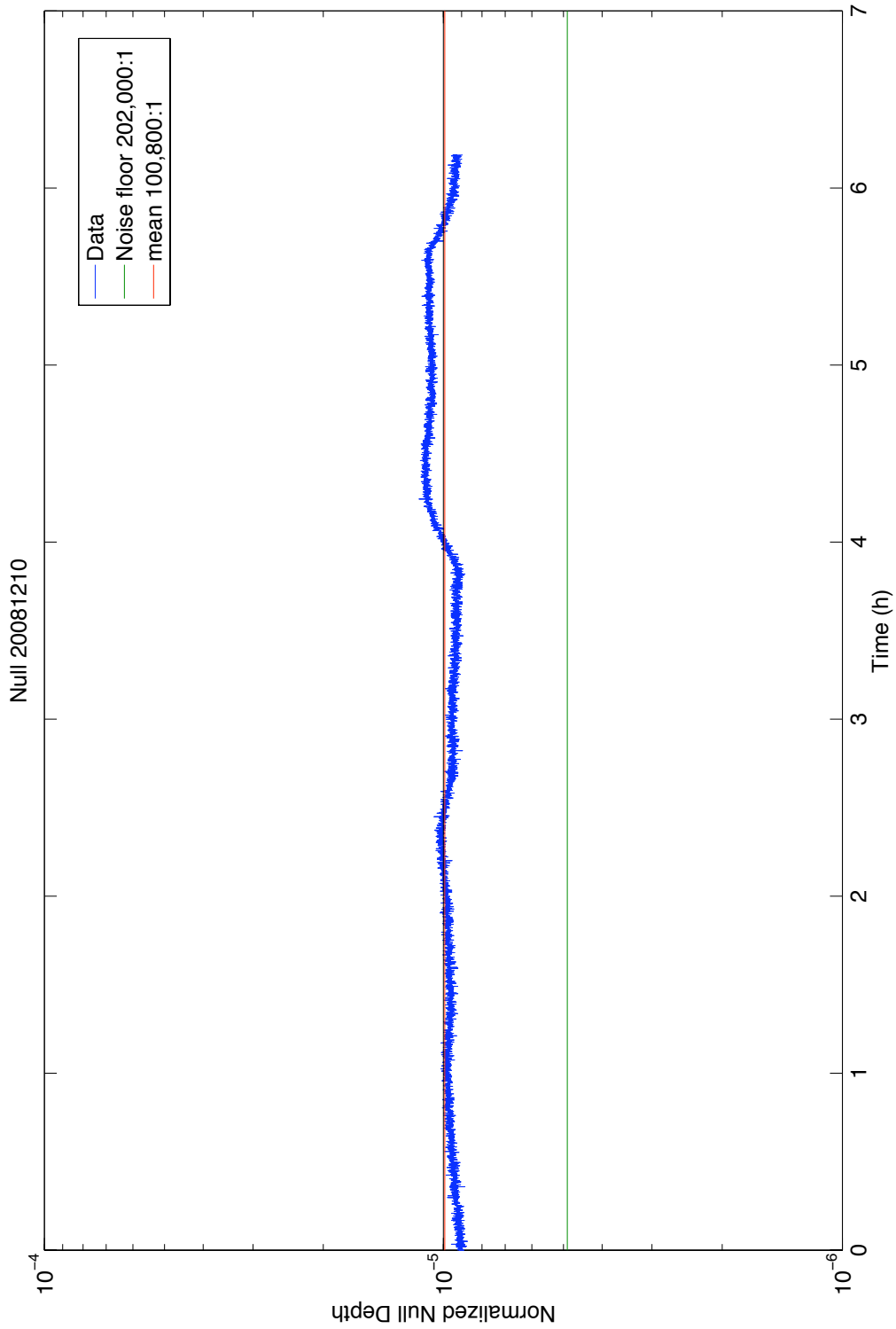
Figure 7: Measured null depth as a function of time, as measured on 10 December 2008. The origin of the time axis ($t = 0$) is shifted from Fig. 6. The mean rejection ratio, as calculated across the entire 6-hour period is 100,800:1.
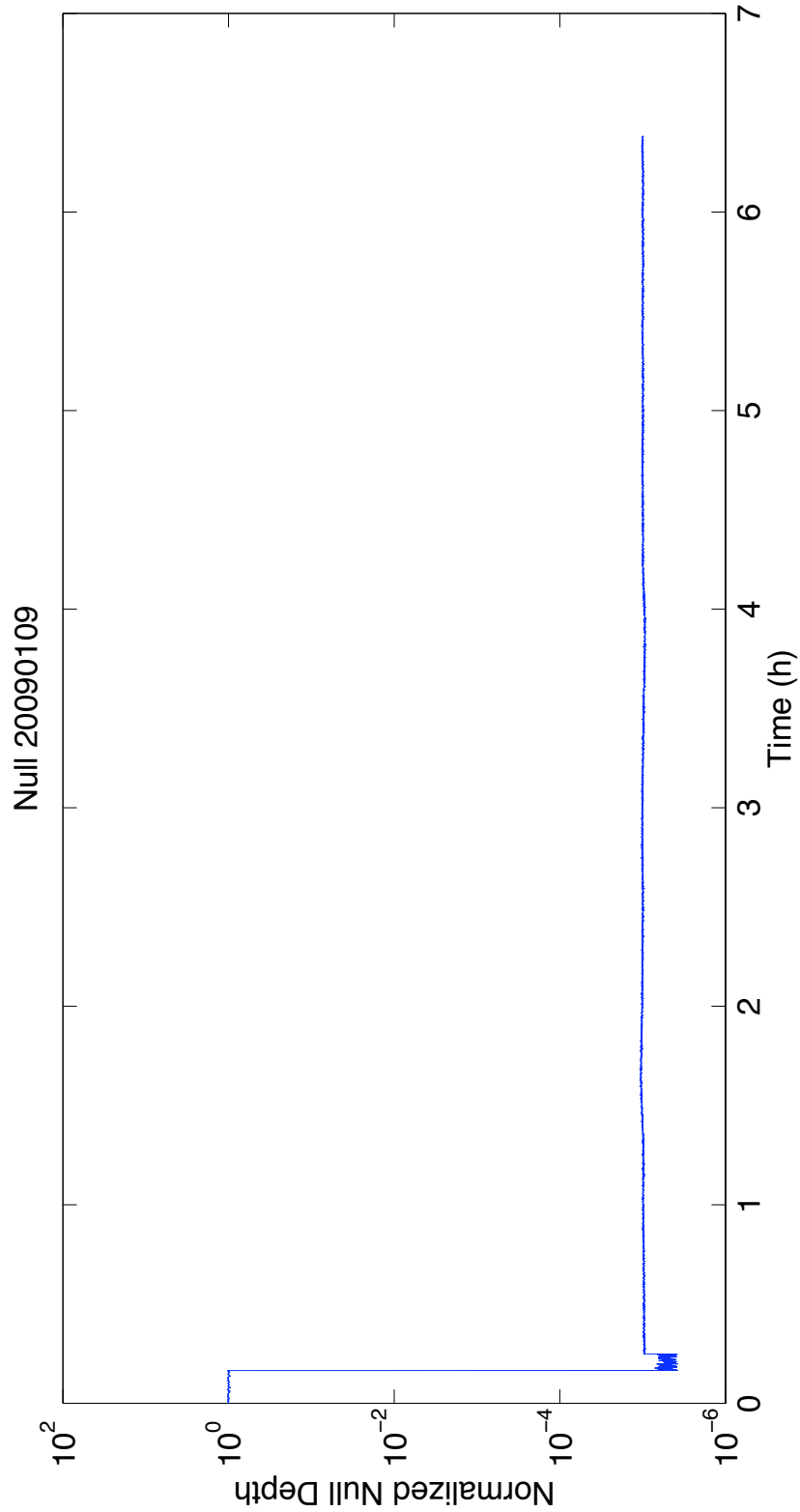
Figure 8: Measured null depth as a function of time, as measured on 9 January 2009. This plot shows the data from the time the experiment was initialized, through until the end of the data taking. An expanded view is shown in Fig. 9.

Figure 9: Measured null depth as a function of time, as measured on 9 January 2009. The mean rejection ratio, as calculated across the entire 6-hour period is 101,000:1.

Figure 10: Measured null depth as a function of time, as measured on 15 January 2009. This plot shows the data from the time the experiment was initialized, through until the end of the data taking. An expanded view is shown in Fig. 11.
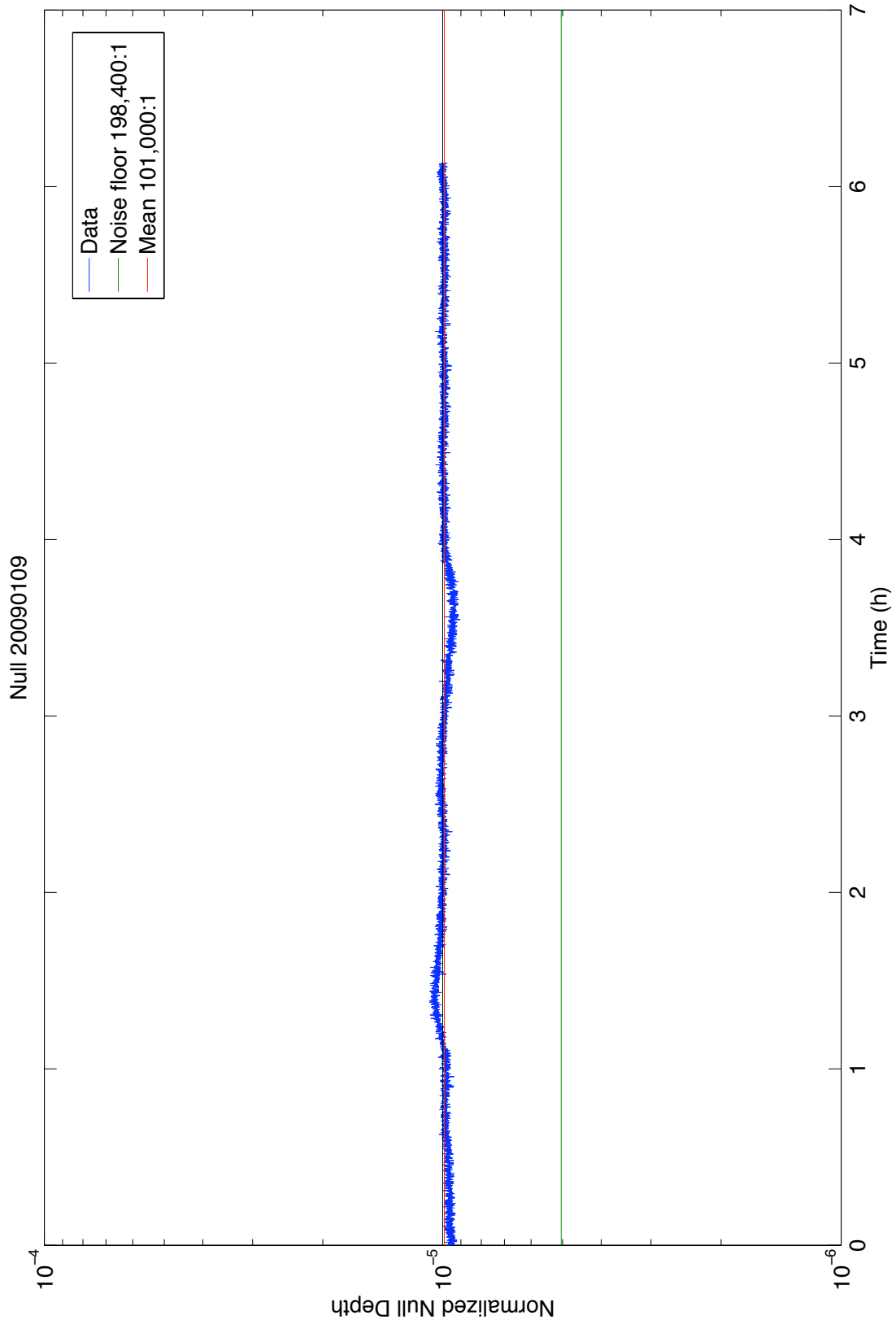
Figure 11: Measured null depth as a function of time, as measured on 15 January 2009. The mean rejection ratio, as calculated across the entire 6-hour period is 101,200:1. The initial bump is due to J. K. Wallace entering the lab.
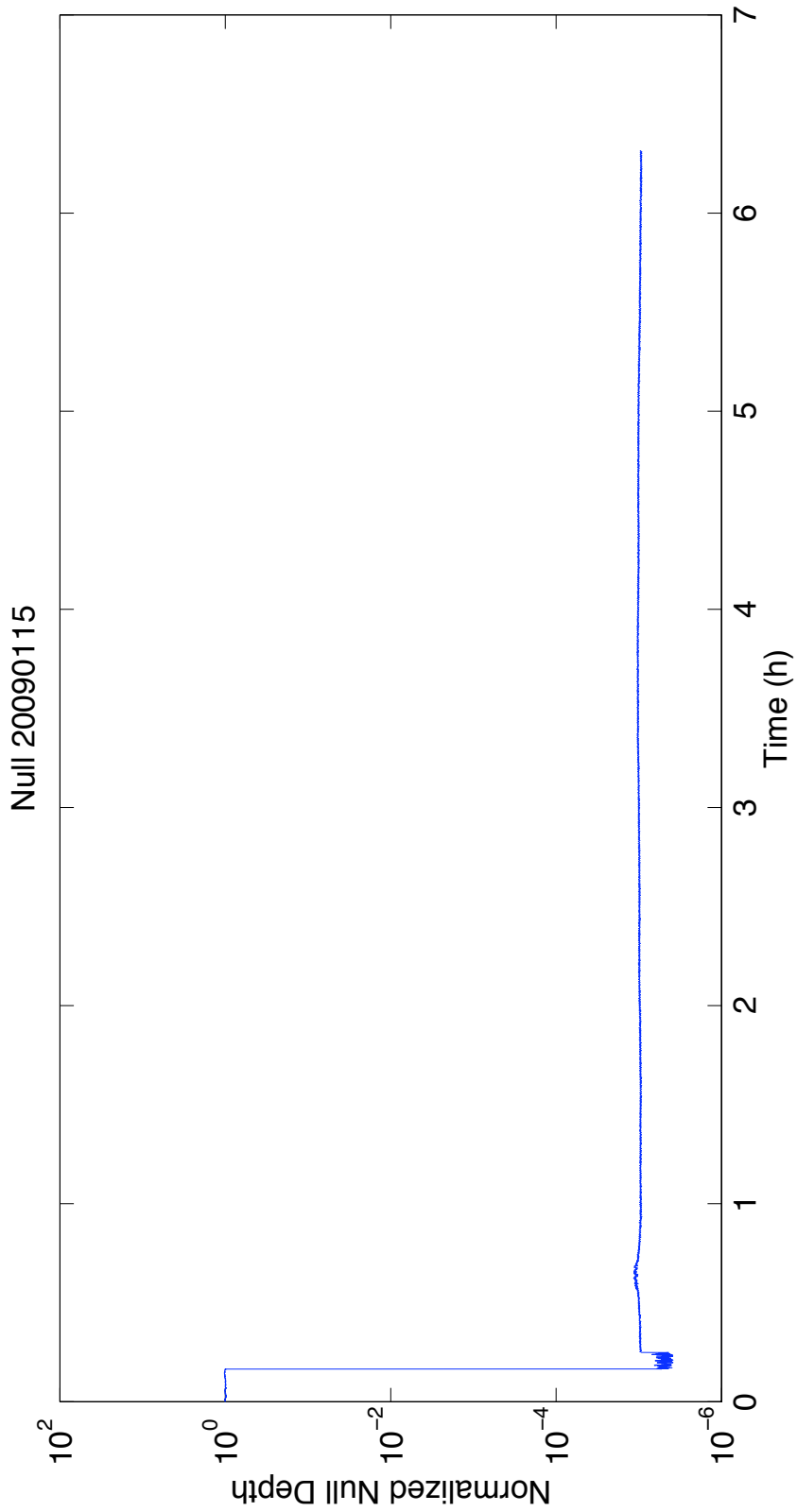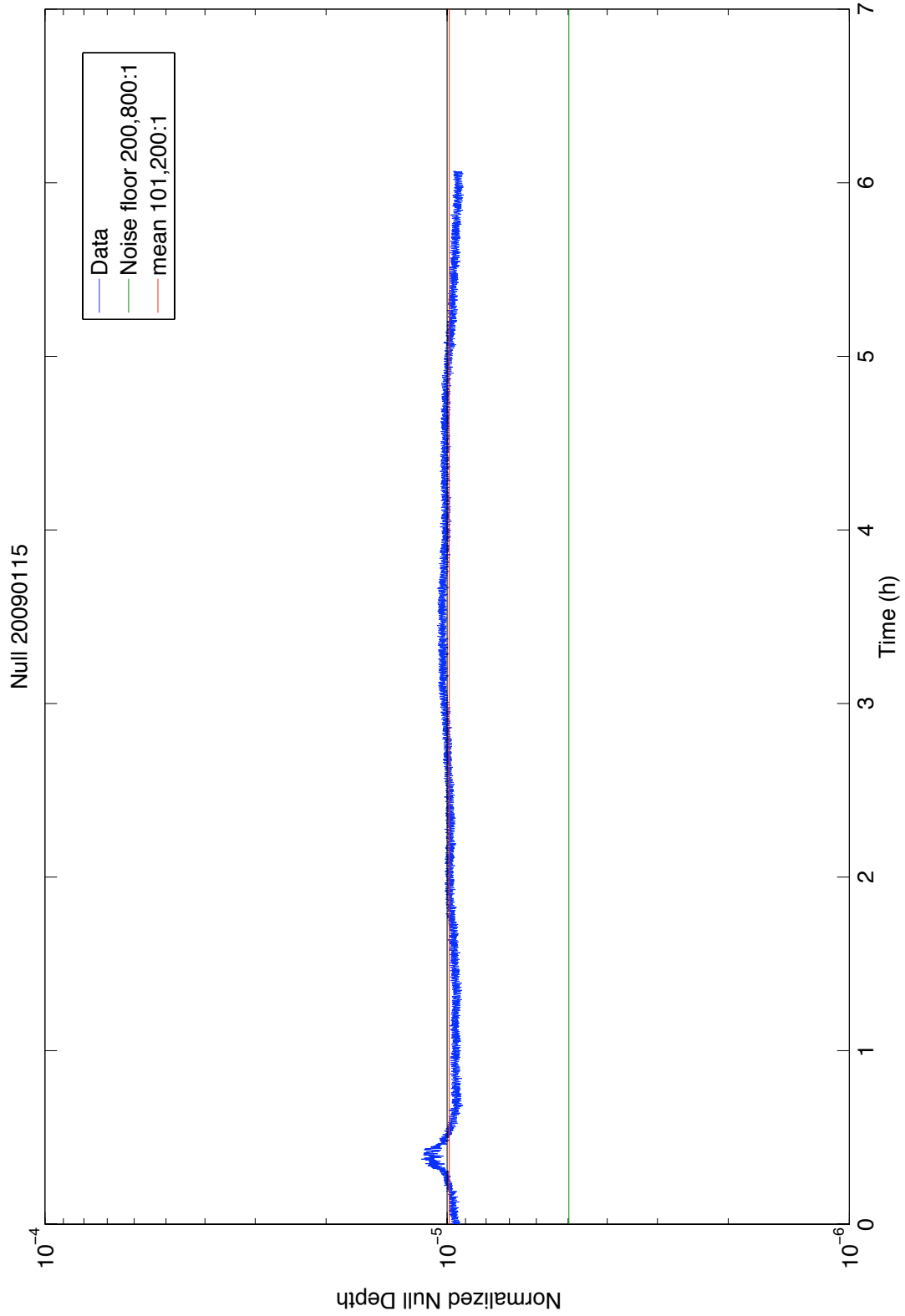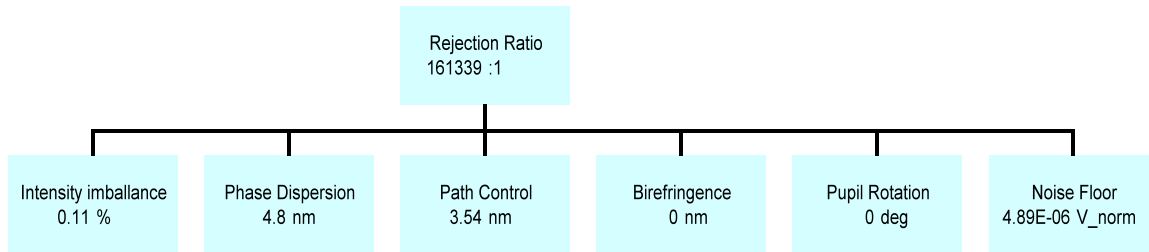
Figure 12. Rudimentary error budget for the Adaptive Nuller milestone results. The Adaptive Nuller produces broadband nulls with a null depth of slightly better than 1×10^{-5}. This is consistent with residuals in intensity, phase, and path control as shown in the error budget. The cumulative effect of the known error sources would limit the null depth to no more than 161,000:1 or 6.2×10^{-6}.

The overall performance of the Adaptive Nuller appears to be reasonably well described by the rudimentary error budget shown in Fig. 12. This error budget does not described the uncertainty in the measurement, but is rather an estimation of the dominant noise sources, and the likely performance limit for nulling. The dominant terms are most likely the residuals in intensity imbalance & phase (as a function of wavelength), path fluctuations, and the noise floor. The residuals in intensity imbalance and phase dispersion arise from the limitations of the adaptive correction. Path control is the residual of the metrology system, and the noise floor is measured for the electronics. Other terms are likely to be less significant. We do not have a measurement of the birefringence or pupil rotation for this testbed. The estimated null depth due to these sources corresponds to a rejection ratio (inverse of null depth) of ~160,000:1. This is within a factor of two of the measured null depths. Other effects notwithstanding, the achievable null depths are yet limited by the noise floor; thus, the current testbed would certainly demonstrate improved performance if it were to operate with less background noise.

7.   Conclusions

This report has described the accomplishment of Milestone #3 and presented results from the Adaptive Nuller testbed.

We conclude that the Exoplanet Interferometry Technology Milestone #3 has been demonstrated. We have restated the success criteria and shown, step by step, that the requirements have been met. We have shown that the broadband null depth can be achieved, demonstrated that the testbed can be stable for at least six hours, and that the tests are repeatable. In summary, all tests performed were shown to be within the requirements set forth for this milestone.

8. Acknowledgements

9. References

R. O. Gappinger, R.T. Diaz, A. Ksendzov, P. R. Lawson, O. P. Lay, K. M. Liewer, F. M. Loya, S. R. Martin, E. Serabyn, and J. K. Wallace, "Experimental evaluation of achromatic phase shifters for mid-infrared starlight suppression," Appl. Opt. **48**, 868–880 (2009).

A. Ksendzov, O. Lay, S. Martin, J. S. Sanghera, L. E. Busse, W. H. Kim, P. C. Pureza, V. Q. Nguyen, and I. D. Aggarwal, "Characterization of mid-infrared single mode fibers as model filters," Appl. Opt. **46**, 7957–7962 (2007).

A. Ksendzov, T. Lewi, O. P. Lay, S. R. Martin, R. O. Gappinger, P. R. Lawson, R. D. Peters, S. Shalem, A. Tsun, and A. Katzir, "Model filtering for midinfrared nulling interferometry using single mode silver halide fibers," Appl. Opt. **47**, 5728–5735 (2008).

P. R. Lawson and J. A. Dooley, Editors, *Technology Plan for the Terrestrial Planet Finder Interferometer*, JPL Pub 05-5 (Jet Propulsion Laboratory: Pasadena, CA, 2005).
http://planetquest.jpl.nasa.gov/Navigator/library/tpfI414.pdf

P. R. Lawson, R. O. Gappinger, R. D. Peters, and O. P. Lay, "TPF-I Technology Milestone #3 Whitepaper: Broadband Starlight Suppression Demonstration," JPL, Pasadena, CA, October 10, 2007.
http://planetquest.jpl.nasa.gov/TPF-I/TPF-I_M3_WhitepaperFinalSignatures.pdf

O. P. Lay, "Removing instability noise in nulling interferometers", Proc. SPIE 6268, 62681A (2006)

R. D. Peters, O. P. Lay, M. Jeganathan, "Broadband phase and intensity compensation with a deformable mirror for an interferometric nuller," Appl. Opt. **47**, 3920–3926 (2008).

Appendix A: Results from the Achromatic Nulling Testbed

The Milestone #3 Whitepaper stipulated that the certification data package include an appendix to document the performance of the other testbed. The main body of the report has documented the performance of the Adaptive Nuller. This appendix documents the performance of the Achromatic Nulling Testbed (ANT). This appendix is not included as part of the success criteria, but is for completeness and information only.

Included here is a reprint copy of the paper

R. O. Gappinger et al. "Experimental evaluation of achromatic phase shifters for mid-infrared starlight suppression," Appl. Opt. 48, 868–880 (2009).

The paper details the performance of the ANT and includes an error budget for single-polarization measurements with the periscope (field-flip using flat mirrors) phase shifter. The paper is reproduced by permission of the Optical Society of America.

Experimental evaluation of achromatic phase shifters for mid-infrared starlight suppression

Robert O. Gappinger,* Rosemary T. Diaz, Alexander Ksendzov, Peter R. Lawson,
Oliver P. Lay, Kurt M. Liewer, Frank M. Loya, Stefan R. Martin, Eugene Serabyn,
and James K. Wallace

Jet Propulsion Laboratory, California Institute of Technology, 4800 Oak Grove Drive, Pasadena,
California 91109, USA

*Corresponding author: Robert.O.Gappinger@jpl.nasa.gov

Phase shifters are a key component of nulling interferometry, one of the potential routes to enabling the measurement of faint exoplanet spectra. Here, three different achromatic phase shifters are evaluated experimentally in the mid-infrared, where such nulling interferometers may someday operate. The methods evaluated include the use of dispersive glasses, a through-focus field inversion, and field reversals on reflection from antisymmetric flat-mirror periscopes. All three approaches yielded deep, broadband, mid-infrared nulls, but the deepest broadband nulls were obtained with the periscope architecture. In the periscope system, average null depths of 4×10^{-5} were obtained with a 25% bandwidth, and 2×10^{-5} with a 20% bandwidth, at a central wavelength of $9.5\,\mu$m. The best short term nulls at 20% bandwidth were approximately 9×10^{-6}, in line with error budget predictions and the limits of the current generation of hardware.   © 2009 Optical Society of America

OCIS codes: 120.3180, 120.4570, 350.1260.

1. Introduction

The Terrestrial Planet Finder (TPF) project has been funded by NASA to develop technology to enable the detection of biosignatures in the spectra of Earth-like exoplanets. Targeted small rocky planets would lie in the habitable zone around a star, where the temperatures are neither too cold nor too hot to preclude life, and where liquid water could exist over geological time scales. However, to observe a statistically significant number of stars, an observatory would potentially need to survey stars out to distances of about 20 pc. Since such planets would subtend angles as small as 40 mas from their parent stars, the diffracted starlight would overwhelm the signal from a planet observed with a typical telescope. The ability to measure spectra of Earth-like exoplanets thus requires not only high angular resolution but also high starlight suppression over a broad bandwidth. One wavelength range in which to observe Earth-like planets is the mid-infrared ($\approx$6–20 μm), where not only are there good biosignatures but also the contrast between stars and planets is more favorable than in the optical regime. However, to provide angular resolution sufficient to separate a planet from its star at mid-infrared wavelengths, a single telescope would require a primary mirror diameter greater than 40 m, and so interferometry, which combines the light from two or more separated telescope apertures, has been adopted as the baseline design approach of both NASA's Terrestrial Planet Finder Interferometer (TPF-I) [1] and the European Space Agency's Darwin [2] projects.

One of the key technology goals of the TPF-I project is thus to demonstrate broadband nulling to the level of 1×10^{-5} or better at mid-infrared wavelengths. If the residual starlight is reduced to that amount, then the dominant sources of noise would be scattered light from our own solar system's

zodiacal cloud and light emitted from an equivalent exozodiacal cloud surrounding a typical target star. It is worth mentioning that the Earth–Sun flux ratio is $\sim10^{-7}$ at a wavelength of $10\,\mu$m, and so another factor of ~100 in background noise rejection is necessary in order to detect Earth-like planets at a reasonable signal-to-noise ratio. This additional rejection, which requires further modulation steps, is not addressed here, but is the subject of ongoing theoretical and laboratory research [3,4].

Interference fringes occur when electromagnetic waves propagating from a source follow different paths and are subsequently recombined. The interference upon recombination produces a spatially varying irradiance distribution, or fringe pattern, which is a function of the relative phase of the two beams. For a broadband source, the fringe pattern is modulated by a coherence envelope. In the absence of dispersion, the maximum in the broadband interference pattern occurs at the center of the envelope, because at that location the fringe phase at each wavelength is identical and a simultaneous constructive coherent addition of the electric field vectors across the whole waveband occurs. This can be achieved in a normal interferometer when the OPD at all wavelengths is reduced to zero; then the phase difference at all wavelengths is identically zero. On the other hand, a nulling interferometer produces a *minimum* in fringe intensity at the center of the coherence envelope [5] because the electric fields in this case cancel each other at all wavelengths across the waveband. For a two-beam interferometer, a central achromatic dark fringe can be achieved if there is an achromatic half-wave, or π, phase shift between incoming beams that is constant across the waveband. The goal of this paper is to evaluate different methods of producing such an achromatic phase shift. Note that some other proposed nulling interferometer arrangements, primarily those with an odd number of telescopes [6], call for achromatic phase shifts other than π rad. This more general case is not under consideration here.

2. Interferometric Nulling

The null depth, N, is defined [7] as the ratio of intensities at adjacent dark, $I_{\min}$, and bright, $I_{\max}$, fringes: $N = I_{\min}/I_{\max}$. This is admittedly a nonideal metric, since only one of the two fringe extrema can in general be achromatic. Nevertheless, with the dark fringe achromatic, there is little error incurred in the ratio by some uncertainty in the constructive peak, and furthermore, this quantity is easily measurable, and so is a very serviceable metric. There are a number of factors that contribute to a degradation of the null depth for a nulling interferometer. Serabyn [7] has described the principal contributors that degrade the null, and following that treatment, the instantaneous null depth can be written as

$$N = \frac{1}{4}\left[(\Delta\Phi)^2 + \langle(\Delta\Phi_\lambda)^2\rangle + (\Delta\Phi_{s-p})^2 + \frac{\pi^2}{4}\left(\frac{\theta_{\mathrm{dia}}}{\lambda_{\mathrm{sh}}/b}\right)^2 \right.$$
$$\left. + (\delta I)^2 + \langle(\delta I_\lambda)\rangle + (\alpha_{\mathrm{rot}})^2 \right], \tag{1}$$

which contains monochromatic and wavelength-dependent terms, the latter notated by a λ subscript. The monochromatic terms include the following: $\Delta\Phi$ is the mean phase difference between the beams in radians, δI is the fractional intensity difference between the two beams, α_{rot} is the relative polarization rotation error in radians, and $\Delta\Phi_{s-p}$ is the birefringent phase difference in radians between the orthogonal polarization states. The wavelength-dependent terms are somewhat more complex. The wavelength-dependent phase difference, $\langle(\Delta\Phi_\lambda)^2\rangle$, is the spectrally weighted phase variance integrated across the passband. The source size term contains the ratio of the angular diameter of the source (θ_{dia}) to the interferometer fringe spacing (λ_{sh}/b) at the shortest wavelength in the passband. Use of the shortest wavelength provides a conservative estimate of this term. These two terms determine how a broadband, spatially extended source contributes to the null depth. As will be discussed in Section 5, the source size term is negligible when single-mode fibers are used in the interferometer. Finally we have the wavelength-dependent intensity difference, $\langle\delta I_\lambda\rangle$, which accounts for spectral intensity differences due to, e.g., beam splitter coatings, mirror imperfections, diffraction, and dispersion. This term is also integrated across the passband.

Experiments in nulling interferometry have been ongoing for about the past 10 years and have been undertaken at visible, near-infrared, and midinfrared wavelengths. Several approaches to achromatic phase shifting have been considered [8] and experimentally tested. The most common variants include (1) using glasses of slightly different thicknesses to introduce a wavelength-dependent dispersive phase delay [9,10], (2) using a through-focus field flip of the light in one arm of the interferometer [11] (the Gouy phase), and (3) using relative field reversals on reflection in an antisymmetric flat-mirror periscope arrangement [5]. In the absence of aberrations, the third is inherently achromatic, the second is only slightly chromatic as a result of reflections off of mirrors of differing radii of curvature, and the first can be made relatively achromatic by tuning. Other techniques are summarized by Serabyn [8], including field reversal by diffraction and polarization methods such as the Pancharatnam phase. Three other approaches to achromatic phase shifting, which are more recent and beyond the scope of this work, are worth drawing to the reader's attention: (1) using a deformable mirror to adjust the intensity and phase in a reimaged spectrum, i.e., adaptive nulling [12], (2) the use of total internal reflections with Fresnel rhombs [13], and (3) the use of a checkerboard spatial distribution [14].

Monochromatic null depths between roughly 1×10^{-7} and 1×10^{-6} have been demonstrated using laser light at visible [4,15,17] and mid-infrared [16] wavelengths. At near-infrared wavelengths nulls have been achieved between 1×10^{-6} and 1×10^{-5} using diode lasers with bandwidths of up to about 5% [18,19]. Wider bandwidth nulling interferometers have attained null depths between 1×10^{-5} and 1×10^{-3}; see, for example, Refs. [16,20–23]. Recently, Samuele *et al.* [15] demonstrated an almost 1×10^{-6} null at visible wavelengths with a bandwidth of 15%. The goals of the work described in this paper were to test and compare the three techniques listed above for achromatic phase shifters at mid-infrared wavelengths, including both performance and ease of setup, alignment, and use, aiming at achieving broadband null depths at roughly the 1×10^{-5} level currently envisioned as necessary for TPF-I.

3. Achromatic Nulling Testbed

The Achromatic Nulling Testbed (ANT) was designed to explore the three different methods of achieving an achromatic π phase shift described above in a single laboratory space. The dispersive glass plates and through-focus methods were the subject of experimental work at JPL prior to 2006, and the dispersive plates method is the technique used in the Keck nuller [4,16,24–26]. The results of that research are summarized only briefly below because much of that work was published earlier. Subsequent work has been devoted to the periscope approach, which is described more fully in the section that follows. A comparison of the results from the different achromatic phase shifting techniques is given in Table 1.

A. Testbed Overview

The three methods were tested in the same laboratory but on different breadboard optical tables that shared the same broadband thermal source. Two key developments that supported all three methods in the suite of testbed work were the installation of a new argon plasma source and the procurement of novel mid-infrared single-mode fibers made from chalcogenide glass. The source layout for the later experiments is shown in Fig. 1.

The null signal for the interferometer is a chopped signal generated with a mechanical chopper wheel located in a focal plane near the infrared source (Fig. 1). The detector is a HgCdTe single pixel detector connected to a preamplifier and a lock-in amplifier. The source is chopped at 100 Hz, which reduces the $1/f$ noise of the detector. In addition, chopping allows us to electronically subtract the thermal background, which would otherwise overwhelm the small interferometric null signal. The chopper wheel driver supplies the lock-in frequency to the electronics.

Because our nulling experiments are performed with room temperature optics, the large thermal background limits the dynamic range of the measurements. Prior mid-infrared nulling experiments at JPL used a ceramic filament as a source. The need for a brighter source led to the development of an argon arc source modeled after the work of Bridges and Migdall [20,27]. This arc source is roughly eight times brighter in the mid-infrared than a 1500 K ceramic filament, thereby increasing the system dynamic range by the same factor. The resultant (random error) dynamic range is set by the ratio of the chopped source signal within a single mode to the background noise reaching the detector and was of the order of 10^6 at 100 Hz. Systematic errors (drifts) turned out to be more of a limitation (see below).

In addition to the broadband source, a CO_2 laser was used for alignment purposes and for verifying the monochromatic performance of the interferometer. The laser is an indispensable tool in isolating different sources of null degradation, in particular distinguishing between achromatic and chromatic effects. Prior mid-infrared laser experiments at JPL had already demonstrated laser nulls better than 1×10^{-6} [16].

Single-mode mid-infrared fibers were manufactured for this work because nulling interferometers under consideration for exoplanet detection would benefit from the spatial filtering and suppression of higher-order optical aberrations provided by the fibers [28]. Use of single-mode fibers allows the tolerances on the optics in the beam train to be lowered and become tractable [29]. Higher-order wavefront aberrations that would otherwise reduce the
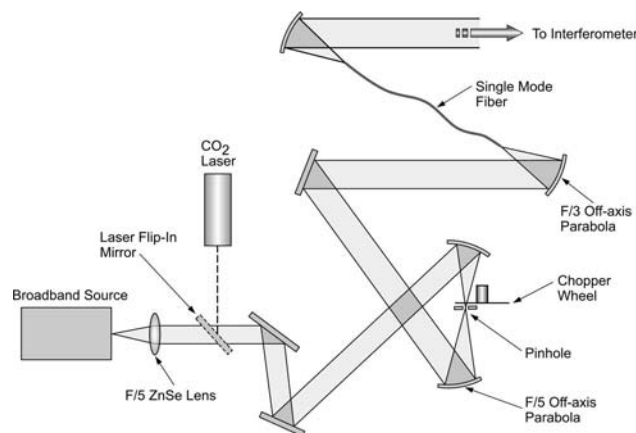
Table 1. Experimental Results for Various Achromatic Nulling Testbed Architectures

Phase Delay Method	Nulling Bandwidth	Polarization	Null Depth (rms)
Single Glass	30%	Dual	8.8×10^{-5}
Dual Glass	30%	Dual	9.1×10^{-5}
Through Focus	25%	Dual	6.7×10^{-4}
Periscope	Laser ($10\,\mu m$)	Dual	1.1×10^{-5}
Periscope	Laser ($10\,\mu m$)	Single	3.3×10^{-6}
Periscope	20%	Single	2.0×10^{-5}
Periscope	25%	Single	4.0×10^{-5}

Fig. 1. Source and input spatial filter layout. CO_2 laser and broadband source are co-aligned into the pinhole and single-mode fiber. Output of the source module is the input to the nuller.

visibility of the fringes (depth of the null) are rejected by the spatial filter. Moreover, errors in tilt in each arm of the interferometer are translated into small errors in received intensity, which are relatively straightforward to correct. The experiments described in this paper make use of single-mode chalcogenide fibers developed for the TPF-I project and tested by Ksendzov *et al.* [29]. For all three versions of the testbed, the output light from the single-mode fiber is collimated by an off-axis parabolic mirror to provide a 25 mm diameter input source beam for the nuller (Fig. 1).

To minimize vibrations and unwanted path length fluctuations, the achromatic phase shifters and interferometers were vibrationally isolated using multiple levels of isolation. Each interferometer was built on an optical breadboard that sat on passive air-filled isolators supported on an optical table. The optical table was floated on compressed-air filled isolation legs. These table legs rested on an isolation pad built into the floor of the laboratory, which has a separate foundation from the rest of the building. In order to minimize acoustic vibrations and the effects of room air flow, each interferometer was surrounded by a plexiglas housing that was supported from the floor of the laboratory. This housing enclosed each interferometer without contacting it. Acoustic vibrations that might otherwise interfere with the measurements were therefore transmitted to the floor.

Finally, note that deep nulling requires a high degree of symmetry, which is most easily achieved by using a beam combiner based on a reversed pair of beam splitters, in, e.g., a modified Mach–Zehnder configuration [6,7]. However, such an arrangement does lead to somewhat increased complexity, and to somewhat lower signal levels (individual signals are a factor of 2 lower in the case of an extra 50/50 beam splitter). On the other hand, since in a laboratory interferometric testbed the source itself first needs to be split in two to provide two equivalent input beams, it is possible to make use of the necessary source beam splitter to provide a simplified laboratory arrangement. In this case the first beam splitter is used to split the source beam, and a reversed beam splitter is used to recombine the beams. This combination of beam splitters of course defines a normal Mach–Zehnder configuration and thus produces exactly the same effect as a modified Mach–Zehnder beam combiner would, i.e., each combining beam sees one beam splitter reflection and one beam splitter transmission. Thus, the desired symmetry is maintained with this simpler system, and so it is possible to make use of a normal Mach–Zehnder configuration in the laboratory with no loss of fidelity.

1. Dielectric Phase Shifters

The first implementation of dispersive phase correctors used a single pair of ZnSe plates to introduce a quasi-achromatic dispersive phase delay. This work followed on the previous experience obtained during development of the nulling combiner of the Keck interferometer [20,21]. The nulling bandwidth for this approach is limited by the wavelength dependence of the phase delay. Experimental results gave rms null depths of 8.8×10^{-5}, which were within approximately a factor of 3 of the 3.7×10^{-5} theoretical limit for a 3-μm bandwidth centered at $10.0\,\mu$m [24].

The successful results obtained using a single-glass dispersive phase delay led to the construction of a dual-glass phase delay architecture [26] as seen in Fig. 2. The overall balancing of chromatic effects obtained using two glasses can extend the π phase shift over a larger bandwidth, or provide a deeper null depth over a narrower bandwidth. The challenge for the dual-glass architecture is the increased complexity involved in optimizing the differential thicknesses of the two glasses. The solution space for two glasses allows very deep nulling over a large range of glass thicknesses but requires fine thickness adjustment in one glass [30]. Thickness adjustments as small as 100 nm are needed to optimize the null.

The dual-glass phase shifter used motorized rotation stages to turn ZnSe and ZnS plates (Fig. 3) of approximately 15 mm thickness with a 2 arcmin wedge. The wedge prevents parasitic fringes due to the Fabry–Perot effect in a plane parallel plate. The optimal thickness differences were calculated with lens design software to give minimum OPD between two beams over the chosen passband. The optimal differential thicknesses for ZnSe and ZnS over our 25% passband centered at $9.5\,\mu$m are 454.03 and $172.48\,\mu$m, respectively. The results vary slightly ($\pm 0.5\,\mu$m thickness difference) depending on the optimization method chosen. Thickness measurements of the glass plates were made using a laser metrology system with submicrometer accuracy [31], showing a thickness difference near optimal for ZnSe of $449.0\,\mu$m but a poorer match of $144.9\,\mu$m for ZnS. The plate rotation required to compensate the thickness error in ZnS was over 7°. This introduced a polarization-dependent intensity imbalance due to Fresnel reflection effects and decreased the thickness adjustment resolution, which is angularly dependent. In addition, deviation from normal incidence introduces beam shear as the glass thickness is adjusted. This beam shear contributes to beam intensity mismatch when coupled into single-mode fiber, thus degrading the null depth.

Theoretical calculations predicted that an ideal dual-glass compensator could produce deeper nulls for a given bandwidth than a single glass. However, this testbed achieved results only comparable to previous single-glass experiments (see Table 1), likely due to the nonideal thickness of the ZnS plates, and the consequent need to rotate the glass plates to nonoptimal angles. The beam shear, glass thickness, and polarization issues can be avoided by using pairs of opposed laterally translatable wedges of glass, as in the case of the Keck interferometer nuller [32], but as this would double the number of glass elements, it has not yet been employed in
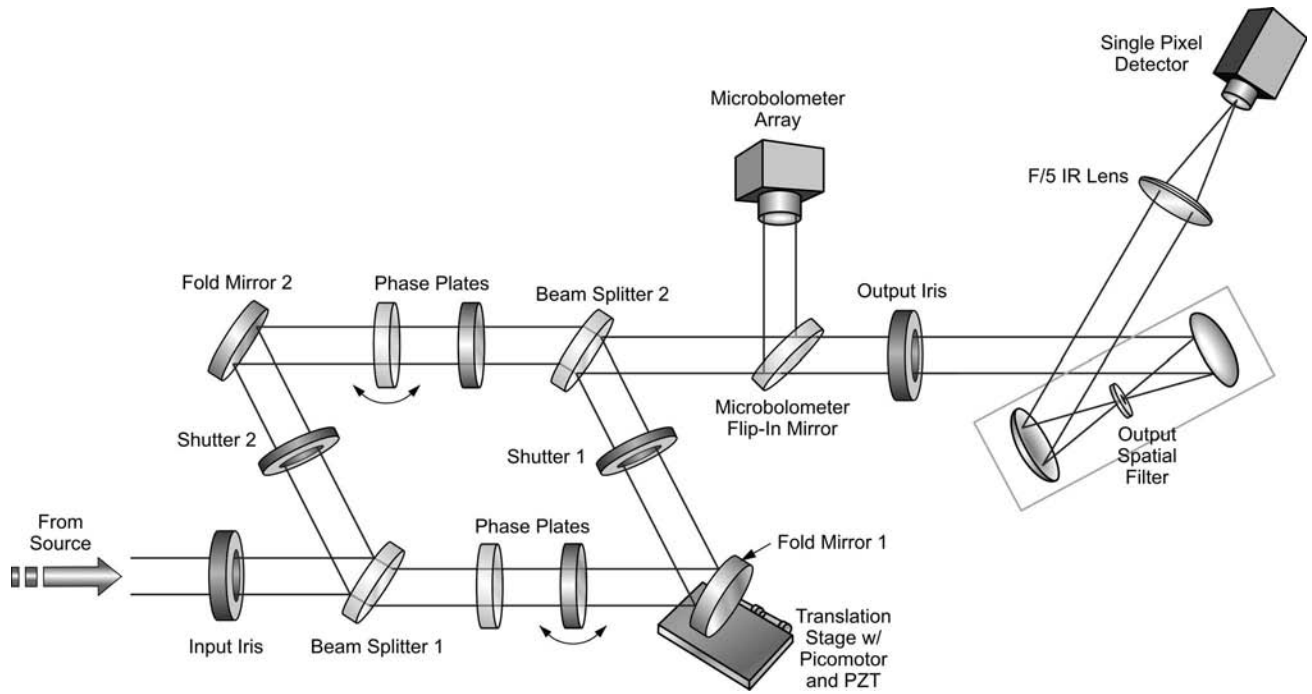
Fig. 2. Phase plate nuller layout. One phase plate in each beam is rotated to optimize the differential glass thickness to generate quasi-achromatic phase shift.

our laboratory testbed work. It is also possible to implement the two-glass solution with two opposing wedges of different materials [19], but this has not been implemented here.

2. Through-Focus Phase Shift (Gouy Phase)

In the through-focus or Gouy phase approach, the beam in one arm of the interferometer is sent through a matched pair of off-axis parabolic (OAP) mirrors and passes through a focus, while the other beam travels the same distance but reflects off plane mirrors. This layout is shown in Fig. 4. The passage through the focus causes a field inversion, which is equivalent to introducing a π phase shift [33,34]. Slight achromaticities may arise due to differing angles on the curved and flat mirrors.

Precise alignment of the OAPs is an extremely important aspect for this approach. The alignment method involved a He–Ne laser boresighted to the
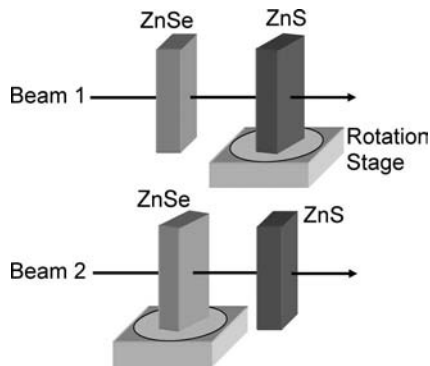

Fig. 3. Dual-glass phase plate adjustment via rotation stages. One plate of each glass type is rotated.

IR beam, target irises, and shear plates. Even so, this method only provided pointing alignment of the interferometer beams to approximately 1 arcmin. In addition, any clocking of the parabolas can lead to imperfect subtraction because of the resultant aberrations and polarization effects. Unfortunately, the use of irises and shear plates during alignment could not effectively determine the relative clocking of the two OAPs to very high accuracy. For example, our lens design software model of the interferometer predicted that a 1° clocking of one OAP produces a combination of astigmatism and coma with a peak-to-valley magnitude of $\lambda/15$ at $\lambda = 9.5\,\mu$m. However, the alignment method we used was found to be insensitive to this amount of clocking, leaving a small amount of differential aberration between the two beams, which can leave a phase error that limits the null depth. A peak-to-valley error of $\lambda/15$ gives approximately $\lambda/50$ rms phase error (0.125 rad rms), which limits the null depth to $\approx 1 \times 10^{-3}$.

The best nulling results for the through-focus interferometer yielded a null depth of only 6.7×10^{-4} over a 25% bandwidth, which was at least a factor of two worse than the previous dispersive glass nulling results [26]. The primary difficulty was the inability to align the system to sufficient accuracy. For this reason it also proved difficult to obtain repeatable results. Successive alignments yielded null depths ranging from 5×10^{-3} to 7×10^{-4}, without any easily discernible difference in the system alignment. The use of through-focus Gouy phase would likely produce better nulls if an improved alignment method, such as a laser Fizeau interferometer, were
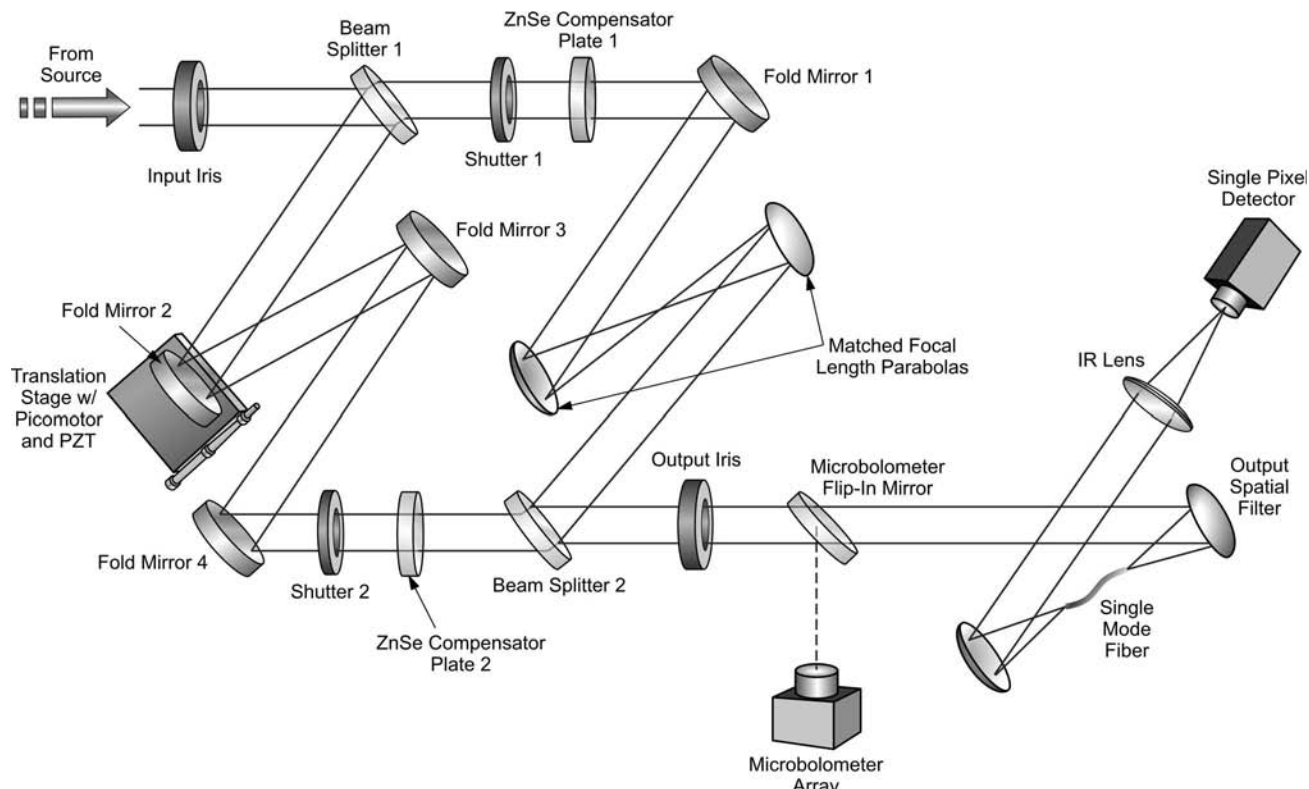
Fig. 4. Through-focus nuller layout. Matched focal length parabolic mirrors provide the mechanism for the Gouy phase shift. The microbolometer array is used to view the infrared beam during alignment.

implemented. It is also possible that longer focal length OAPs might reduce the sensitivity to misalignment, and thereby improve the achievable null depths.

4. Periscope Phase Shifter and Nuller

The periscope phase shifter [5] has no powered optics in the arms of the interferometer and is therefore easier to align. The phase shift is accomplished through an electric field flip (or pupil inversion) of one pupil relative to the other within an antisymmetric periscopelike arrangement of mirrors, as shown in Fig. 5. The periscope layout is fully antisymmetric, and because of the geometric nature of the field flip, the π phase shift is intrinsically achromatic for matched optical trains. Our field inversion periscope is composed of four mirrored prisms optically bonded to a single glass block, referred to here as the periscope monolith. Because this approach yielded the best results, we now discuss it in more detail.

A. Input and Output Optics

The periscope nuller used single-mode spatial filters both at the input and the output. Each spatial filter is composed of two OAP mirrors with a single-mode mid-infrared fiber made from chalcogenide glass in between. The single-mode chalcogenide fiber has a core diameter of $23\,\mu m$ and a cladding diameter of $170\,\mu m$. Characterization of the fibers was done at JPL by Ksendzov *et al.* [29]. As shown in Fig. 1, an OAP mirror focuses light from the broadband source onto the single-mode fiber and the output of this fiber

is collimated using another OAP. The first spatial filter is used at the interferometer input to provide a broadband artificial star that is spatially coherent (i.e., an unresolved point source). This input fiber is not strictly required, although it greatly simplifies the alignment tolerances by reducing sensitivity to beam shear. The beam is then steered into the nuller as shown labeled "From Source" in Figs. 6 and 7.

The CO_2 laser and arc sources, which were common to all ANT layouts, were effectively co-aligned by means of injection into the same single-mode fiber. This guarantees that the laser and broadband sources are injected into the interferometer identically. The second spatial filter is implemented at
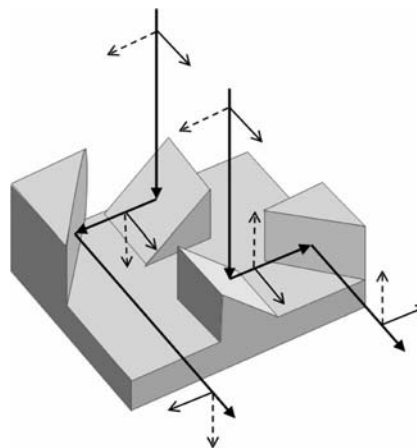

Fig. 5. Electric field (pupil) inversion in the periscope nulling architecture.

the output of the interferometer. This additional chalcogenide fiber filters the wavefronts in the combined beam. Tilt errors between the interferometer arms are converted to an intensity mismatch when the beams are coupled into the single-mode fiber at the output.

B. Mach–Zehnder Interferometer

As noted earlier, to simplify the layout, our laboratory nulling architecture is essentially a classical Mach–Zehnder interferometer. In the case of the periscope architecture, the periscope field flip optics are then located between the two beam splitters. The source and input optics, including a single-mode fiber, are shown in Fig. 1. The overall layout of the interferometer is shown in Fig. 6, and a close-up of the input beam splitter (Beam splitter 1) and the periscope monolith is shown in Fig. 7. Light from a broadband infrared source is transferred through the single-mode fiber, as illustrated in Fig. 1, and directed upward to Beam splitter 1, shown in Figs. 6 and 7. The two resulting beams are reflected down into the periscope monolith where the electric field inversion is performed as illustrated in Fig. 5. One interferometer beam reflects off the piston mirror, which is driven by laser metrology for implementation of path length (phase) control via a picomotor and piezoelectric transducer (PZT) on a translation stage. The two interferometer beams are combined at Beam splitter 2 and the nulled output is then directed to the output single-mode fiber and HgCdTe detector.

C. Dispersion Compensation

The only transmissive components required in the interferometer are two ZnSe beam splitters. These beam splitters have, potentially, a difference of up to $4\,\mu$m in their respective optical thicknesses because of manufacturing tolerances and thus introduce different amounts of chromatic dispersion into each beam. Since the beam splitters have a 2 arcmin wedge, differences in beam height at each beam splitter will add to the effective differential glass thickness. Left uncorrected, a $4\,\mu$m difference would limit the null depth to 2.8×10^{-5} for a 25% passband centered at $9.5\,\mu$m (Fig. 8). A discussion of the beam splitter effects and design can be found in Martin *et al.* [16]. The actual beam splitter thickness differences were not measured, but residual dispersion in the interferometer indicates a glass thickness difference of as much as $8\,\mu$m. Manufacturing tolerances alone do not account for this difference, and thus the effect is likely due to the glass wedge angle. Beam centration on the beam splitters was not a major driver during alignment, and observations indicate up to 10 mm difference between the position on the first and second beam splitters. To compensate for the resultant dispersion, wedged ZnSe compensator plates were included in each interferometer beam, which can be rotated with respect to each other to match the beam splitter differential optical thickness. Equalizing the amount of ZnSe in each beam path to better than $1\,\mu$m, in theory allows a null depth of 1.7×10^{-6}. The dispersion
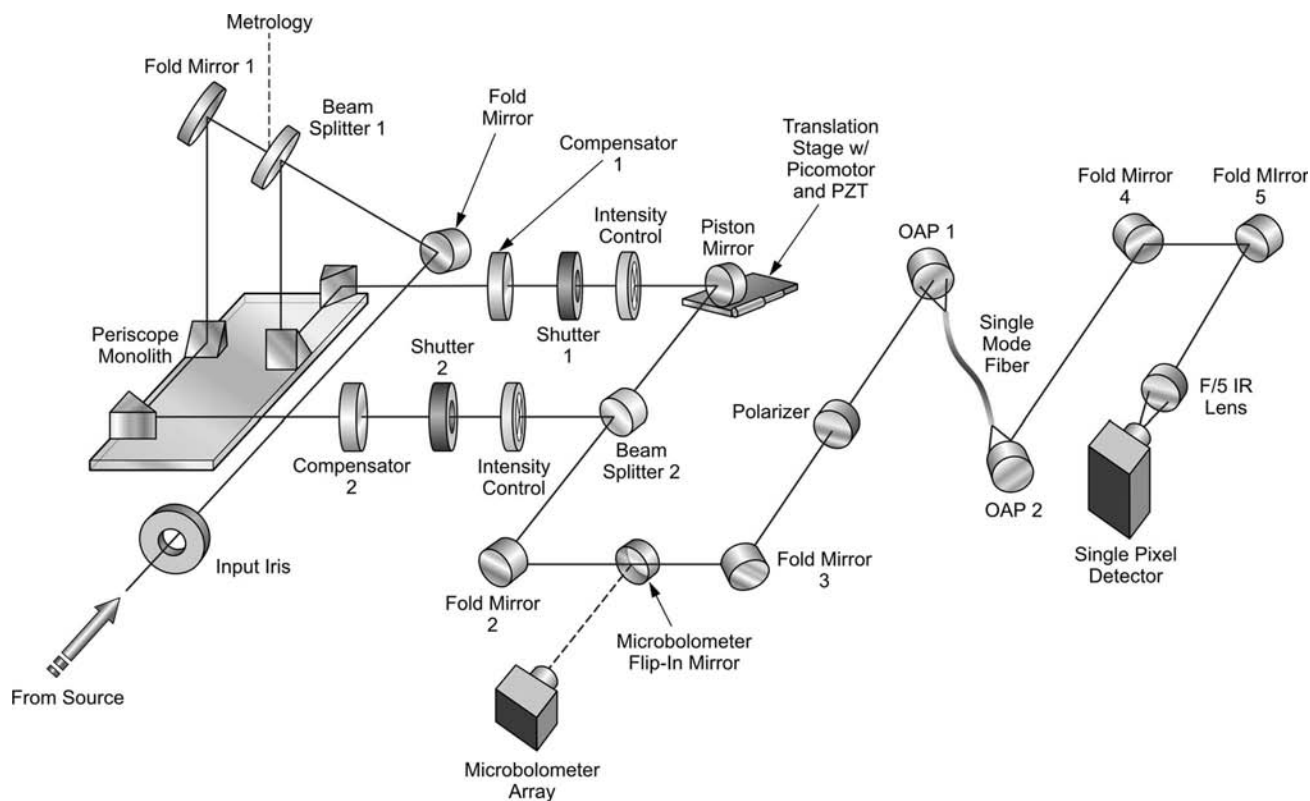

Fig. 6. Periscope nuller layout. Note, the metrology beam enters from the top (back side of Beam splitter 1) and exits to a separate detector (not shown) from the back side of Beam splitter 2.
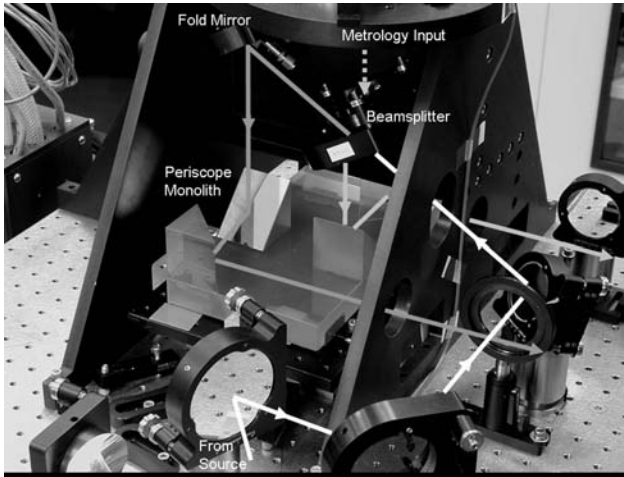
Fig. 7. Photograph of the periscope nulling interferometer including Beam splitter 1 and the field flip mirrors in the periscope monolith.

compensating plates are shown in the interferometer layout of Fig. 6.

D. Intensity and Phase Control

One of the most important requirements for a deep null is equal intensities in the two beams, so a precise means of adjusting the actual intensity is needed. The degree of required control is discussed below. Intensity balancing is accomplished by the insertion of a pair of crossed wires in each beam, which are moved laterally by a picomotor translation stage to differentially adjust the intensity. (Note, this adjustment does not provide control of wavelength-dependent amplitude differences, which may be present due to different beam splitter coatings, diffraction effects, or other sources within the interferometer.)

Phase control is split up into several contributions. The OPD between the arms of the interferometer is affected by vibration (high frequency), thermal drifts (low frequency), and dispersion (static). While nulling, the phase difference between the interferometer arms is maintained using an active control loop to drive the piston mirror in Beam 1. Although the passive vibration isolation effectively minimizes the higher frequency OPD effects, a laser-based hetero-
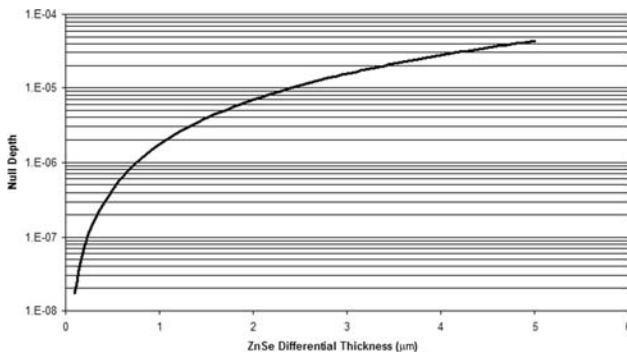
dyne metrology control system operating at 633 nm is used to actively control the OPD for frequencies below 10 Hz. The metrology control loop operates at a 100 kHz sampling rate and a 10 kHz control bandwidth. A 1 mm diameter metrology beam is injected through the back side of Beam splitter 1 decentered by approximately 5 mm from the infrared optical axis as shown in Fig. 7. This allows the metrology signal to measure the OPD along virtually the same path as the broadband infrared beam. The metrology beam is combined with a local oscillator, and the resultant signals are detected from the back side of Beam splitter 2.

5. Error Budget for the Periscope Nuller

As introduced earlier, Eq. (1) expresses the primary factors affecting nulling performance. For the single-polarization case discussed here, we can neglect the polarization term, $\Delta\Phi_{s-p}$. We used two infrared polarizers with a rejection ratio of 10^{-4} each to achieve a total linear polarization purity of $\sim 10^{-8}$. Table 2 summarizes the factors affecting null depth on the periscope nuller, the measured level of control, and the estimated contribution to null depth for each factor. These factors are discussed in detail in the following sections.

A. Polarization Rotation

An alignment error within the periscope monolith would cause a polarization rotation error. This rotation can also be understood as a pupil rotation. To achieve a null of 1×10^{-5} for the system, the pupil rotation must be within 3 mrad of π. This turns out to be relatively easy to accomplish during construction of the periscope monolith. An autocollimator was used to monitor alignment of each mirror surface of the monolith. The mirrors were optically contacted to a glass base plate to form the monolith. Using a wet optical contacting method allowed each mirror to be adjusted to 15 arcsec tolerance [35], at least a factor of 4 better than the pupil rotation error requirement.

Alignment of the incidence angle at the beam splitters is a much more difficult process. Due to the three-dimensional layout of the periscope nuller, errors in alignment angle result in shear and path length errors through the monolith. Also, differences in reflectance angle on the two beam splitters may cause wavelength-dependent intensity differences in the beams. An autocollimator, a coordinate measurement arm, and mechanical alignment targets were used to align the interferometer such that the incidence angles on the two beam splitters matched to within 2 arcmin. Broadband beam splitter coatings are generally insensitive to incident angle changes of this magnitude. Based on this modeling, the wavelength-dependent intensity effects should be negligible. In addition, the alignment method ensured that the beams exiting the monolith were parallel to better than 1 arcmin, and each mirror surface within the monolith was correct to within

Fig. 8. Null depth versus differential glass thickness. Bandwidth for calculation is 25% centered at 9.45 μm.

Table 2. Contributing Factors for Single-Polarization Null Depth on Periscope Nuller

Parameter	Equation	Achieved Tolerance	Null Depth Allocation
Intensity balance	$\frac{1}{4}(\delta I)^2$	0.25%	1.6×10^{-6}
Path length control	$\frac{1}{4}(\Delta\Phi)^2$	3.0 nm rms	1.0×10^{-6}
Differential glass thickness	$\frac{1}{4}(\Delta\Phi_\lambda)^2$	1.0 μm	1.7×10^{-6}
Pupil rotation	$\frac{1}{4}(\alpha_{\text{rot}})^2$	3 mrad	3.6×10^{-7}
Fiber cladding	$\sim(r)^{-2}$	$r = 1000$	$\sim 1.0 \times 10^{-6}$
Polarization phase delay	$\frac{1}{4}(\Delta\Phi_{s-p})^2$	$\sim$10 nm rms	$\sim 1.0 \times 10^{-8}$
Spectral intensity difference	$\frac{1}{4}(\Delta I_\lambda)^2$	0.25% (model)	3.3×10^{-8}
Broadband source size	$\frac{\pi^2}{16}\left(\frac{\theta_{\text{dia}}}{\frac{\lambda}{b}}\right)^2$	Single-mode fiber, point source	0
Predicted single polarization null (arithmetic sum of null contributions)			5.7×10^{-6}
Best measured single polarization null			9×10^{-6}

1 arcmin of the nominal 45° angle. For a statistically likely case, in which all four monolith components have opposite 30 arcsec angular errors, the resultant pupil rotation difference between interferometer arms is 2 arcmin (1.2 mrad). We can therefore allocate a tolerance of pupil rotation of $\alpha_{\text{rot}} = 1.2 \times 10^{-3}$ rad. This allocation alone would limit the null depth to a negligible contribution of $(1/4)\,\alpha_{\text{rot}}^2 = 3.6 \times 10^{-7}$.

B. Intensity and Phase Balance

As mentioned previously, beam intensity balance is controlled with thin wires in each beam. Measurement of the individual beam power for the interferometer arms shows that adjustment of the wires allows the average intensity difference to be controlled to better than 0.25%. If we set $\delta I = 2.5 \times 10^{-3}$, this residual intensity difference alone should limit the achievable null depth to $N_{\delta I} = (1/4)(\delta I)^2 = 1.6 \times 10^{-6}$.

The heterodyne metrology system provides data on both the passive path length control through vibration isolation and the active path control when the control loop is on. Calculation of the cumulative rms phase error from open loop metrology data indicates that the passive vibration isolation provides residual optical path stability of 2–3 nm rms for frequencies above 10 Hz, as shown in Fig. 9. Performing the same calculation on closed loop metrology data shows that OPD control maintains the same 2–3 nm rms path stability for frequencies below 10 Hz. If we set $x = 3$ nm in $\Delta\Phi = (2\pi/\lambda)x$, this level of path fluctuation alone should limit the achievable null depth to $N_{\Delta\Phi} = (1/4)(\Delta\Phi)^2 = 1.0 \times 10^{-6}$.

The rotation, intensity, and phase terms considered above are all monochromatic contributions to the null. Given that the best measured monochromatic (laser) null measured on the periscope nuller is $N_{\text{laser}} = 3.3 \times 10^{-6}$, the agreement with the sum of the three estimated monochromatic contributions, 3.0×10^{-6}, is excellent. This monochromatic laser null is a factor of a few worse than earlier CO_2 laser work [16], because the goals of the ANT were not deep laser nulls per se. Instead, the laser only needed

to be nulled to a level below that required by the broadband experiments to follow.

C. Chromatic Dispersion

In addition to monochromatic terms, there are two wavelength-dependent terms that contribute to degradation of the null. The first is chromatic dispersion due primarily to thickness differences in the beam splitter and recombiner that must be accounted for. As described previously, ZnSe compensator plates are used to balance this dispersion. A differential glass thickness will cause the broadband fringe envelope to be asymmetric about the central null fringe. The asymmetry can be adjusted by rotating the compensator plates to balance the intensity of the fringes immediately adjacent to the central null. (Alternatively, a long-scan Fourier transform can be used, but this technique, when implemented, proved no more sensitive than the balancing of fringe minima.) A corrected fringe asymmetry of approximately 2% was routinely achievable, which corresponds to a differential glass thickness calculated to be approximately 1 μm. The index of refraction of ZnSe at $\lambda = 10$ μm is 2.4, and therefore the null fringe would be found when 1 μm of ZnSe is matched with
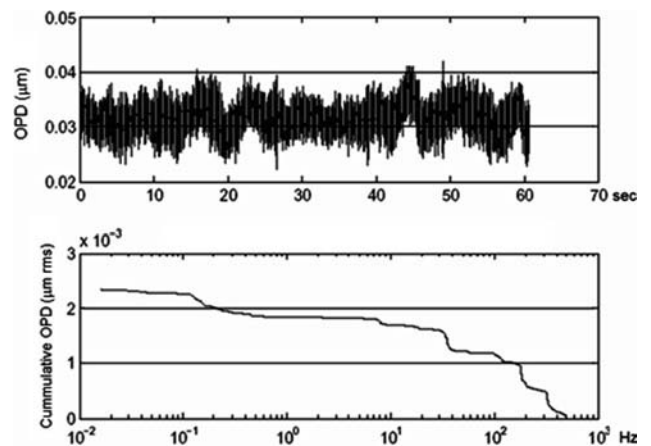

Fig. 9. Metrology data showing path length stability. The upper trace shows the raw, unprocessed metrology signal, indicating the real-time path length stability. The lower trace shows the cumulative rms path difference as a function of vibration frequency.

2.4 μm of air path. This glass mismatch introduces a phase slope across the passband, and if we assume that the phase difference is identically zero at the center of the band ($\lambda_{center} = 9.5\,\mu m$, 25% bandwidth), then there is an rms phase of $\Delta\Phi_\lambda = 2.6 \times 10^{-3}$. If all other effects were perfectly compensated, this would limit the null depth to $(1/4)(\Delta\Phi_\lambda)^2 = 1.7 \times 10^{-6}$.

The second wavelength-dependent term is the chromatic intensity difference between beams. This difference may be a result of beam splitter or mirror reflectivity differences. We did not have a means by which to measure the chromatic intensity difference between the interferometer beams, but the effect can be modeled in software. Since the monochromatic intensity difference is effectively an average across the waveband, we expect any chromatic difference to be equal or less in magnitude than the monochromatic term. Allowing a 0.25% linear slope in intensity across a 25% bandpass, centered at $9.45\,\mu m$, produces a null depth limitation of only 3.3×10^{-8}.

D. Source Size and Single-Mode Fibers

The spatial coherence of the broadband source is another limiting factor for the null depth. The source size term in Eq. (1) indicates that both the source spatial extent and the interferometer spatial resolution contribute to this effect. With ideal single-mode fibers on the input and output of the interferometer there would be no contribution from this term—the Mach–Zehnder experiment configuration has an effective interferometer baseline b of zero (both arms sample the same piece of wavefront), and an ideal input fiber has a source diameter of $\theta_{dia} = 0$ [28].

Furthermore the use of an ideal single-mode fiber as an output spatial filter translates the phase distribution in the pupil plane into its single average phase value within the fiber. With appropriate amplitude (beam intensity) control, an ideal output spatial filter therefore creates an opportunity for perfect nulling. However, in practice, insufficient higher-order mode suppression of the fibers may be a limiting factor. For the chalcogenide fibers used here, the fiber cladding modes are suppressed by a rejection factor of 1000 [29]. Since stray light from the cladding may add incoherently to the null signal at the detector, this suppression factor is important for realizing deep, low-noise nulls.

There are two potential sources of light in the fiber cladding: first, light from the source image on the input fiber tip that falls outside of the fiber core area, and second, aberrated light that arrives at the second fiber tip outside of the core of the ideal point-spread function (due to aberrations in the interferometer optics). In the first case, light from our broadband argon arc source is focused onto a $60\,\mu m$ pinhole, which is then imaged onto the input fiber tip with a magnification of 0.6. If all light from the $36\,\mu m$ pinhole image that does not couple into the $23\,\mu m$ core is instead coupled into the cladding, then the irradiance in the cladding is approximately equal to that in the core. Assuming no net loss of cladding modes in the interferometer, the cladding light is suppressed by a factor of $r = 1000$ per fiber. The result is a null contribution of $N_{clad} \approx r^{-2} \approx 10^{-6}$. In the second case, only one fiber is traversed by the aberrated light generated within the interferometer. Based on the surface quality of the ANT optics, the rms wavefront error is likely to be about $0.03\,rad$ rms at $10\,\mu m$, so that approximately 0.1% of the light would couple into the output fiber cladding. The resulting null depth contribution would thus again be $\sim 10^{-6}$. Thus, while more uncertain than some of the other terms discussed, the cladding leakage likely does not provide a major limitation.

E. Polarization Delay

Due to the orientation of beam splitters in the interferometer there is a built-in orientation for s and p polarization. From the symmetry of the design, in the ideal case, one would expect no net phase difference between the two polarizations. In practice we found an estimated 10–15 nm difference in path length for the s and p polarizations. This measurement was performed using a gold wire grid infrared polarizer. The metrology system was used to hold the interferometer at the null fringe while the polarizer was rotated through 90°. Metrology piston control was then moved in 10 nm steps to again minimize the null fringe. This polarization dependent path length difference is reflected in the nulling results shown in Table 1. Allocating $x_{s-p} = 10\,nm$, we have $\Delta\Phi_{s-p} = (2\pi/\lambda)\,x_{s-p} = 1.1 \times 10^{-5}$. We consistently observed deeper nulls with a polarizer in place than without. While there are methods for introducing polarization rotation, such as using the Pancharatnam phase [36], no method of adjusting the polarization phase difference was included in this testbed. In order to achieve the deepest nulls, the broadband experiments were limited to single-polarization nulling.

F. Error Budget Summary

Table 2 summarizes the expected error budget for single-polarization nulling measurements taken at 20% bandwidth. The parameters, alignment tolerances, and calculations are as expressed in Eq. (1). Several of the resultant error budget terms are similar, ~ 1–2×10^{-6}, so no single term dominates the resultant error budget. The net error budget yields an estimate for the best possible null depth of $\sim 6 \times 10^{-6}$, although it must be remembered that several of the terms entering this sum are rather rough estimates.

6. Periscope Nuller Results

The periscope nuller consistently yielded $10\,\mu m$ laser single-polarization null depths of the order of 5×10^{-6}, with best average values of 3.3×10^{-6}. The laser nulls were used primarily as a diagnostic tool to confirm that monochromatic effects were controlled to the desired levels. The best single-polarization broadband nulls achieved to date with the periscope nuller are displayed in Figs. 10 and

11. Both the 20% and the 25% bandwidth data were obtained using infrared bandpass filters with a center wavelength of $9.45\,\mu$m. The only change to the interferometer between the two data sets was the bandpass filter used. The data show average nulls of 2×10^{-5} for 20% bandwidth and 4×10^{-5} for 25% bandwidth, with a few best nulls of the order of 9×10^{-6} for the 20% case. The null clearly drifts slowly and regularly between $\sim 9 \times 10^{-6}$ and 3–4×10^{-5}. This slow drift is also present in "dark" data, shown in Fig. 12, suggesting that a low level electronic drift or instability is limiting the long-term average null depths attainable with white light to $\sim 10^{-5}$. This drift is not as much a limiting factor for laser measurements, because of the higher signal levels. Nevertheless, even in the presence of this drift, the best short-term nulls seen, $\sim 9 \times 10^{-6}$, are very close to the prediction of the error budget, $\sim 6 \times 10^{-6}$.

7. Conclusion

Of the three nulling approaches that were examined, the periscope nuller yielded the best broadband single-polarization nulls. This may have been the result of the inherently achromatic architecture of this phase shifter, however this nuller was implemented within an interferometer that used potentially dispersive elements: a matched beam splitter/recombiner pair with an inevitable thickness difference. The best nulling results obtained with the periscope nuller are quite close to the null depth predicted by a detailed error budget, and the attainable long-term average null is limited by a slight electronic instability or drift at approximately the 10^{-5} level. These broadband nulls are, to our knowledge, the best broadband mid-infrared nulling results achieved to date without the use of active optics. The periscope nuller has thus been able to demonstrate performance levels close to those demanded by mid-infrared terrestrial exoplanet observations. Of course as a result, the performance already exceeds that required for nulling observations of Hot Jupiters [37].

The performance of the other two approaches tested might also have yielded improved results had the testbeds been equipped with higher-
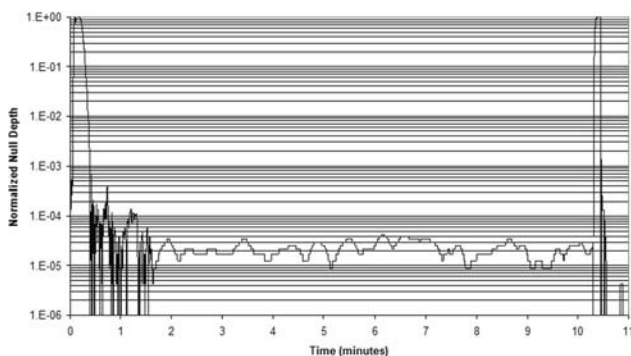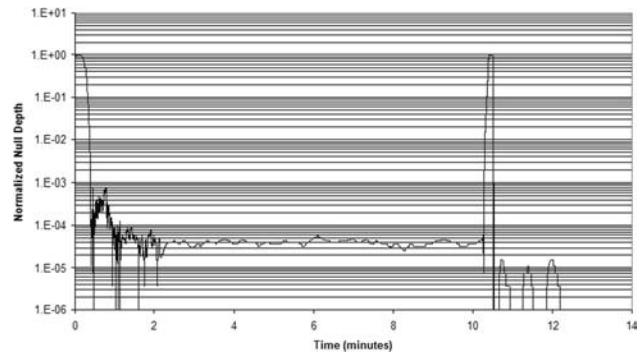

Fig. 11. Null fringe measurement for 25% bandwidth, centered at $9.45\,\mu$m.

resolution alignment techniques. The limitations in the dual-glass approach were attributed to insufficient resolution in the adjustment of differential glass thickness. In particular, opposed pairs of wedged glass elements [32] can provide improved thickness resolution and would also remove many other issues from the table (such as beam shear and polarization effects). The limitations in the through-focus approach, attributed to insufficient resolution in pointing and clocking alignment, can of course also be improved upon. Accurate alignment and balancing of the relevant parameters is of course critical to the success of any nuller, and as pointed out earlier, symmetry and stability are paramount [6,7]. It should also be noted that both these architectures were implemented in a dual polarization arrangement. Given the polarization limitations in the periscope nuller, it is possible that single-polarization measurements for the dual-glass and through focus methods could have yielded comparable results.

In parallel with this research, work in adaptive nulling has also been conducted at JPL [12], which has yielded null depths of 1.1×10^{-5} at 32% bandwidth, slightly exceeding the performance reported here. In fact, the static and active methods of compensation are complementary, in that the stroke of active nulling components is limited, especially in relation to long mid-infrared wavelengths. Thus, a

Fig. 10. Null fringe measurement using a bandpass filter with a full width at half-maximum width of 20%, centered at $9.45\,\mu$m. The fringe signal is normalized to the constructive peak signal.
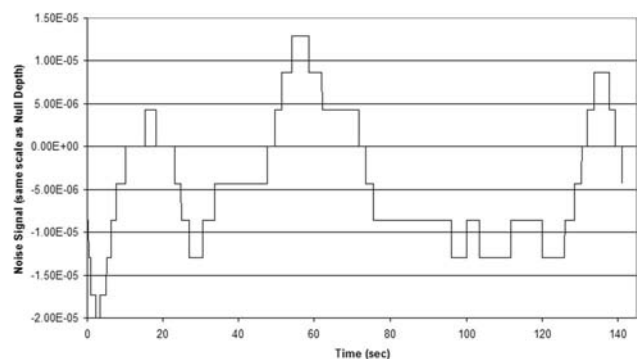

Fig. 12. Electronic noise on the periscope nuller. The vertical scale is the same as the null measurements. This is the signal measured by the detector and electronics with the infrared source blocked.

flight nulling system would likely rely on both types of nuller, with a classical broadband nuller to get within the stroke range of the final active nulling stage. Thus, assuming such a hybrid approach, many of the necessary phase shifting capabilities needed for a TPF-I-like flight system have been demonstrated to approximately the levels required for exoplanet observations in the mid-infrared.

References

1. P. R. Lawson, O. P. Lay, S. R. Martin, R. D. Peters, R. O. Gappinger, A. Ksendzov, D. P. Scharf, A. J. Booth, C. A. Beichman, E. Serabyn, K. J. Johnston, and W. C. Danchi, "Terrestrial Planet Finder Interferometer: 2007–2008 progress and plans," Proc. SPIE **7013**, 70132N (2008).
2. C. S. Cockell, T. Herbst, A. Leger, M. Fridlund, T. Herbst, L. Kaltenegger, O. Absil, C. Beichman, W. Benz, M. Blanc, A. Brack, A. Chelli, L. Colangeli, H. Cottin, V. Coude du Foresto, W. Danchi, D. Defrere, J.-W. den Herder, C. Eiroa, J. Greaves, T. Henning, K. Johnston, H. Jones, L. Labadie, H. Lammer, R. Launhardt, P. Lawson, O. P. Lay, J.-M. LeDuigou, R. Liseau, F. Malbet, S. R. Martin, D. Mawet, D. Mourard, C. Moutou, L. Mugnier, F. Paresce, A. Quirrenbach, Y. Rabbia, J. A. Raven, H. J. A. Rottgering, D. Rouan, N. Santos, F. Selsis, E. Serabyn, H. Shibai, M. Tamura, E. Thiebaut, F. Westall, White, and J. Glenn, "Darwin—A mission to detect and search for life on extrasolar planets," Astrobiology, available at http://arxiv.org/abs/0805.1873.
3. O. P. Lay, "Removing instability noise in nulling interferometers," Proc. SPIE **6268**, 62681A (2006).
4. S. Martin, P. Szwaykowski, and F. Loya, "Testing exo-planet signal extraction using the Terrestrial Planet Finder Planet Detection Testbed," Proc. SPIE **5905**, 590508 (2005).
5. E. Serabyn and M. M. Colavita, "Fully symmetric nulling beam combiners," Appl. Opt. **40**, 1668–1671 (2001).
6. B. Mennesson, A. Leger, and M. Ollivier, "Direct detection and characterization of extrasolar planets: The Mariotti space interferometer," Icarus **178**, 570–588 (2005).
7. E. Serabyn, "Nulling interferometry: symmetry requirements and experimental results," Proc. SPIE **4006**, 328–339 (2000).
8. E. Serabyn, "Nulling interferometry progress," Proc. SPIE **4838**, 594–608 (2003).
9. R. Angel, "Use of a 16 m telescope to detect earth-like planets," in *The Next Generation Space Telescope*, P. Bely, C. Burrows, and G. Illingworth, eds. (Space Telescope Science Institute, 1989), p. 81.
10. R. M. Morgan, J. H. Burge, and N. J. Woolf, "Final laboratory results of visible nulling with dielectric plates," Proc. SPIE **4838**, 644–655 (2003).
11. P. Baudoz, J. Gay, and Y. Rabbia, "Interfero-coronagraphy: a tool for detection of faint companions," Astron. Soc. Pac. Conf. Ser. **134**, 254–261(1998).
12. R. D. Peters, O. P. Lay, and M. Jeganathan, "Broadband phase and intensity compensation with a deformable mirror for an interferometric nuller," Appl. Opt. **47**, 3920–3926 (2008).
13. D. Mawet, C. Hanot, C. Lenaerts, P. Riaud, D. Defrere, D. Vandormael, J. Loicq, K. Fleury, J.-Y. Plesseria, J. Surdej, and S. Habraken, "Fresnel rhombs as achromatic phase shifters for infrared nulling interferometry," Opt. Express **15**, 12850–12865 (2007).
14. D. Rouan and D. Pelat, "The achromatic chessboard, a new concept of a phase shifter for nulling interferometry. I. Theory," Astron. Astrophys. **484**, 581–589 (2008).
15. R. Samuele, J. K. Wallace, E. Schmidtlin, M. Shao, B. M. Levine, and S. Fregoso, "Experimental progress and results of a visible nulling coronagraph," in *Proceedings of IEEE Aerospace Conference* (Institute of Electrical and Electronic Engineers, 2007), paper 1333.
16. S. R. Martin, R. O. Gappinger, F. M. Loya, B. P. Mennesson, S. L. Crawford, and E. Serabyn, "A mid-infrared nuller for Terrestrial Planet Finder: design, progress, and results," Proc. SPIE **5170**, 144–154 (2003).
17. P. Haguenauer and E. Serabyn, "Deep nulling of laser light with a single-mode-fiber beam combiner," Appl Opt **45**, 2749–2754 (2006).
18. K. Ergenzinger, R. Flatscher, U. Johann, R. Vink, and Z. Sodnik, "EADS Astrium nulling interferometer breadboard for Darwin and GENIE," in *Proceedings of the International Conference on Space Optics 2004* (European Space Agency, 2004), pp. 223–230.
19. C. Buisset, X. Rejeaunier, Y. Rabbia, and M. Barillot, "Stable deep nulling in polychromatic unpolarized light with multi-axial beam combination," Appl. Opt. **46**, 7817–7822 (2007).
20. J. K. Wallace, G. Hardy, and E. Serabyn, "Deep and stable interferometric nulling of broadband light with implications for observing planets around nearby stars," Nature **406**, 700–702 (2000).
21. B. Mennesson, S. L. Crawford, E. Serabyn, S. Martin, M. Creech-Eakman, and G. Hardy, "Laboratory performance of the Keck Interferometer nulling beam combiner," in *Towards Other Earths: Darwin/TPF and the Search for Extrasolar Terrestrial Planets* (European Space Agency, 2003), Vol. SP-539, pp. 525–529.
22. A. J. Booth, S. R. Martin, and F. Loya, "Exoplanet exploration program, planet detection test-bed: latest results of planet light detection in the presence of starlight," Proc. SPIE **7013**, 701320 (2008).
23. B. Mennesson, P. Haguenauer, E. Serabyn, and K. Liewer, "Deep broad-band infrared nulling using a single-mode fiber beam combiner and baseline rotation," Proc. SPIE **6268**, 626830 (2006).
24. J. K. Wallace, V. Babtiwale, R. Bartos, K. Brown, R. Gappinger, F. Loya, D. MacDonald, S. Martin, J. Negron, T. Truong, and G. Vasisht, "Mid-IR interferometric nulling for TPF," Proc. SPIE **5491**, 862–873 (2004).
25. J. K. Wallace, R. Bartos, R. Gappinger, F. Loya, S. Moser, and J. Negron, "Progress in broadband infrared nulling technology for TPF," Proc. SPIE **5905**, 590505 (2005).
26. R. O. Gappinger, J. K. Wallace, R. D. Bartos, D. R. MacDonald, and K. A. Brown, "Current progress on TPFI nulling architectures at Jet Propulsion Laboratory," Proc. SPIE **5905**, 590506 (2005).
27. J. M. Bridges and A. L. Migdall, "Characterization of argon arc source in the infrared," Metrologia **32**, 625–628 (1996).
28. B. Mennesson, M. Ollivier, and C. Ruilier, "Use of single-mode waveguides to correct the optical defects of a nulling interferometer," J. Opt. Soc. Am. A. **19**, 596–602 (2002).
29. A. Ksendzov, O. P. Lay, S. Martin, J. S. Sanghera, L. E. Busse, W. H. Kim, P. C. Pureza, V. Q. Nguyen, and I. D. Aggarwal, "Characterization of mid-infrared single-mode fibers as modal filters," Appl. Opt. **46**, 7957–7962 (2007).
30. F. Brachet, A. Labeque, A. Leger, M. Ollivier, C. Lizambert, V. Hervier, B. Chazelas, B. Pellet, T. Lepine, and C. Valette, "Nulling interferometry for the Darwin mission: polychromatic laboratory test bench," Proc. SPIE **5491**, 991–998 (2004).

31. O. Lay, S. Dubovitsky, R. Peters, J. Burger, W. Steier, S. Ahn, and H. Fetterman, "MSTAR: an absolute metrology system with submicrometer accuracy," Proc. SPIE **5491**, 1068–1078 (2004).

32. E. Serabyn, A. J. Booth, M. M. Colavita, M. J. Creech-Eakman, S. L. Crawford, J. Garcia, R. L. Johnson Jr., E. Hovland, C. Koresko, E. R. Ligon III , S. R. Martin, B. P. Mennesson, J. D. Moore, D. L. Palmer, C. G. Paine, M. Shao, M. R. Swain, R. F. Smythe, and G. Vasisht, "The Keck Interferometer Nuller: system architecture and laboratory performance," Proc. SPIE **5491**, 806–815 (2004).

33. J. Gay and Y. Rabbia, "Principe d'un coronagraphe interférentiel," *Comptes Rendus de l'Academie des Sciences Paris*, Serie II b, Astronomical Techniques (1996), Vol. 322, pp. 265–271.

34. L. G. Gouy, "Sur une propriété nouvelle des ondes lumineuses," C. R. Acad. Sci. **110**, 1251–1253, (1890).

35. R. O. Gappinger, R. T. Diaz, S. R. Martin, F. M. Loya, and P. R. Lawson, "Current progress on TPF-I mid-infrared achromatic nulling at the Jet Propulsion Laboratory," Proc. SPIE **6693**, 669318 (2007).

36. W. J. Tango and J. Davis, "Application of geometric phase techniques to stellar interferometry," Appl. Opt. **35**, 621–623 (1996).

37. W. Danchi and B. Lopez, "The Fourier-Kelvin Stellar Interferometer (FKSI)—A practical infrared space interferometer on the path to the discovery and characterization of Earth-like planets around nearby stars," C. R. Phys. **8**, 396–407 (2007).